HIGHLIGHTS

- Middle Triassic shoshonitic magmatism in the Dolomites, Southern Alps
- Linking the metasomatized Finero phlogopite peridotite to the shoshonitic magmatism
- Exhaustion of the slab-derived signature inherited from the Variscan subduction

The Variscan subduction inheritance in the Southern Alps Sub-Continental Lithospheric Mantle: clues from the Middle Triassic shoshonitic magmatism of the Dolomites (NE Italy)

Casetta F.[1*], Ickert R.B.[2,3], Mark D.F.[3,4], Giacomoni, P.P.[1], Bonadiman C.[1], Ntaflos T.[5], Zanetti A.[6] and Coltorti M.[1,7]

[1]Department of Physics and Earth Sciences, University of Ferrara, Via Saragat 1, 44121 Ferrara, Italy

[2]Department of Earth, Atmospheric, and Planetary Sciences, Purdue University, 550 Stadium Mall Drive, West Lafayette, IN 47907

[3]Scottish Universities Environmental Research Centre, Rankine Avenue, East Kilbride, G75 0QF, UK

[4]Department of Earth and Environmental Science, University of St Andrews, St Andrews, KY16 9AJ, UK

[5]Department of Lithospheric Research, University of Vienna, Althanstraße 14 (UZA II), 1090 Wien, Austria

[6]Istituto di Geoscienze e Georisorse - C.N.R., Unità di Pavia (Italy)

[7]Istituto Nazionale di Geofisica e Vulcanologia (INGV) Sezione di Palermo, Palermo, Italy

* Corresponding author. Phone +39 0532 974721. E-mail: cstfrc@unife.it

The Variscan subduction inheritance in the Southern Alps Sub-Continental Lithospheric Mantle: clues from the Middle Triassic shoshonitic magmatism of the Dolomites (NE Italy)

Abstract

Although often speculated, the link between the Middle Triassic shoshonitic magmatism at the NE margin of the Adria plate and the subduction-related metasomatism of the Southern Alps Sub-Continental Lithospheric Mantle (SCLM) has never been constrained. In this paper, a detailed geochemical and petrological characterization of the lavas, dykes and ultramafic cumulates belonging to the shoshonitic magmatic event that shaped the Dolomites (Southern Alps) was used to model the composition and evolution of the underlying SCLM in the time comprised between the Variscan subduction and the opening of the Alpine Tethys. Geochemical models and numerical simulations enabled us to define that 5-7% partial melting of an amphibole + phlogopite-bearing spinel lherzolite, similar to the Finero phlogopite peridotite, can account for the composition of the primitive Mid-Triassic SiO_2-saturated to -undersaturated melts with shoshonitic affinity ($^{87}Sr/^{86}Sr_i$ = 0.7032-0.7058; $^{143}Nd/^{144}Nd_i$ = 0.51219-0.51235; Mg #~ 70; ~1.1 wt% H_2O). By taking into account the H_2O content documented in mineral phases from the Finero phlogopite peridotite, it is suggested that the Mid-Triassic SCLM source was able to preserve a significant enrichment and volatile content (600-800 ppm H_2O) for more than 50 Ma, i.e. since the slab-related metasomatism connected to the Variscan subduction. The partial melting of a Finero-like SCLM represents the exhaustion of the subduction-related signature in the Southern Alps lithosphere that predated the Late Triassic-Early Jurassic asthenospheric upwelling related to the opening of the Alpine Tethys.

Keywords

Southern Alps Sub-Continental Lithospheric Mantle; Subduction-related metasomatism; Middle Triassic shoshonitic magmatism; Finero phlogopite peridotite

1. Introduction

The genesis of shoshonitic magmas is controversial, as it can be variably ascribed to syn- to post-collisional tectonic settings or to subduction-related geodynamic contexts (e.g., Conticelli et al., 2009; Peccerillo and Frezzotti, 2015). The typical Large-Ion Lithophile Elements (LILE), Light Rare Earth Elements (LREE) enrichments and High Field Strength Elements (HFSE) depletion of shoshonitic rocks, coupled with the recorded radiogenic $^{87}Sr/^{86}Sr$ and unradiogenic $^{143}Nd/^{144}Nd$ ratios, always reflects enrichment of the underlying Sub-Continental Lithospheric Mantle (SCLM) domains (Conceição and Green, 2004; Zheng, 2019). Shoshonitic melts are thought to be generated by SCLM portions modified by the interaction with slab-derived fluids or melts, or crustal recycled lithophile components (Plank, 2014; Zheng, 2019), and can be powerful tools to track the composition and evolution of the lithosphere during major geodynamic cycles.

In this regard, of paramount interest is the Middle Triassic (242-237 Ma) occurrence of shoshonitic magmatism in the Dolomites (NE Italy; Fig. 1) and throughout the Southern Alps (see Lustrino et al., 2019). The Mid-Triassic magmatism of the Southern Alps is particularly interesting because of its timing, that is in between two major geodynamic episodes, i.e. the Variscan subduction (430-340/300 Ma) and the Late Triassic/Early Jurassic opening of the Alpine Tethys (Stampfli et al., 2013; Kroner and Romer, 2014). This last rifting phase was marked by a strong asthenospheric upwelling that induced the production of highly alkaline anorogenic magmas at 225-215 Ma throughout the Southern Alps, i.e. 20 Ma after the termination of the shoshonitic magmatic cycle (Stahle et al., 2001; Casetta et al., 2019).

Notwithstanding its concomitance with dominant strike-slip to extensional tectonics (e.g., Doglioni, 2007), the Mid-Triassic magmatic event that shaped the Dolomites was historically

79 defined as “shoshonitic” due to the potassic affinity/orogenic-type of the magmatic products
80 (Sloman, 1989; Casetta et al., 2018a; 2018b; Lustrino et al., 2019). Despite its geodynamic
81 implications, this term was adopted throughout the text to indicate the magmatic affinity, in line
82 with previous studies, although multiple and articulated geodynamic/tectonic models for the
83 Southern Alps magmatism have been proposed so far. They include: i) aborted continental
84 rifting (Bernoulli and Lemoine, 1980); ii) sinistral strike-slip tectonics (Doglioni, 2007); iii)
85 arc/back-arc systems located at the Paleotethys NW limb (Zanetti et al., 2013); iv) subduction
86 of a Palaeozoic oceanic basin located between Austroalpine and Southern Alps (Bianchini et
87 al., 2018); v) reactivation, during an anorogenic rifting phases, of old SCLM domains
88 metasomatized during the Variscan subduction (Sloman, 1989; Bonadiman et al., 1994; De Min
89 et al., 2020).
90 Although the impact of the Variscan subduction on the Southern Alps/Austroalpine SCLM
91 portions is widely documented, as in case of the Finero and Ulten peridotitic massifs (Zanetti
92 et al., 1999; Tumiati et al., 2003; Ionov et al., 2017; Giovanardi et al., 2020), a direct link
93 between the metasomatic event and the subsequent genesis of magmas with orogenic-like
94 affinity is still missing, feeding relevant questions:
95 - What was the composition of the Southern Alps SCLM during Middle Triassic?
96 - How did this mantle source evolve from the Variscan subduction to the Alpine Tethys
97 opening?
98 - In which way is Mid-Triassic shoshonitic magmatism related to the geochemical features
99 of the Southern Alps SCLM?
100 To contribute in answering these questions, a geochemical and petrological investigation of
101 mafic to intermediate lava flows, dykes and entrained ultramafic cumulates cropping out in the
102 Dolomites was put forward. These products, located close to the coeval Predazzo Intrusive
103 Complex (Fig. 1; Casetta et al., 2018a; 2018b), belong to the acme of the Mid-Triassic
104 magmatism (from 239.04±0.04 to 237.58±0.04; Storck et al., 2020), which was typified by the

emission of effusive products recording a mantle-derived signature, with limited crustal contamination (Storck et al., 2020). These volcanic sequences are ideal objects for investigating the evolution of the Southern Alps SCLM, and modelling its possible links to the main geodynamic processes recorded in the neighbouring orogenic peridotites (Zanetti et al., 1999; Tumiati et al., 2003). Mineral phase, whole-rock major and trace element analyses and Sr-Nd isotopes were used to constrain the *T-P* path of shoshonitic magmas during ascent and differentiation, as well as to model the nature of the Southern Alps SCLM during Mid-Triassic. Numerical models were performed to: i) reconstruct the composition of the primitive magmas in equilibrium with potential mantle sources; ii) trace the evolution of the SCLM beneath Adria during Mid-Triassic, in the large context of what recorded in the Finero, Balmuccia, Baldissero and Ulten peridotitic massifs; iii) determine the geometry of the feeding system and the main processes that led to ascent/differentiation of the shoshonitic magmas in the crust.

2. Geological setting

The Mid-Triassic magmatic event that took place throughout the Southern Alps between ~243 and 227±6 Ma was characterized by the emission of significant amounts of igneous rocks with calc-alkaline to shoshonitic affinity (Lustrino et al., 2019; Storck et al., 2020 and references therein). In the central and eastern Southern Alps, an earlier volcanoclastic phase, with discountinuous emission of acidic products was followed by a dominantly effusive stage, characterized by the eruption of mafic lavas and emplacement of shallow intrusive bodies (Bonadiman et al., 1994; Casetta et al., 2018a; Storck et al., 2020). The oldest magmatic manifestations, i.e. tuff layers embedded in the sedimentary Buchenstein Fm. in the Brescian Alps, record zircon U-Pb ages of 242.65±0.04 Ma, whereas the youngest episodes, represented by tuff layers inside the Wengen Fm. in the Dolomites, yield an age of 237.58±0.04 Ma (Wotzlaw et al., 2018; Storck et al., 2020).

130 The most productive phase of the Mid-Triassic magmatic event is best preserved in the thick
131 sequences of mafic to mildly evolved volcanics of the Dolomites (Fig. 1), emplaced after an
132 earlier (242.01±0.05 Ma) phreatomagmatic episode recorded by lapilli tuffs and tuff deposits.
133 The effusive phase lasted <0.9 Ma (Storck et al., 2020), and was characterized by the production
134 of submarine pillow lavas, pillow breccias, lava breccias, hyaloclastites, and subaerial lava
135 flows, rarely intercalated with volcanoclastic sandstones. The production of volcanites was
136 associated to the emplacement of articulated dyke swarms and plutonic bodies, which are in
137 magmatic contact with the overlying lava flows and/or cut by dykes with the same composition
138 of the volcanites (Casetta et al., 2018b).
139
140 **3. Materials and methods**
141 The volcanic products (lava flows and lava breccias) and dykes crop out in the Dolomites, and
142 are spatially associated to the Predazzo Intrusive Complex (Fig. 1). Due to the widespread
143 hydrothermal alteration affecting the magmatic products in this area, an initial collection of
144 more than 200 samples was reduced to ~50 specimens for the purposes of this study, after
145 detailed screening based on thin section observations. The least altered samples were selected
146 for detailed whole-rock and in-situ chemical determinations. Whole-rock major and trace
147 element chemistry was determined by means of an ARL Advant-XP automated X-Ray
148 Fluorescence (XRF) spectrometer hosted at the Department of Physics and Earth Sciences of
149 the University of Ferrara. Full matrix correction procedure and intensities were completed
150 following Traill and Lachance (1966). Accuracy and precision were better than 2-5% for major
151 elements and 5-10% for trace elements. Detection limits were 0.01 wt% and 1-3 ppm for most
152 of the major and trace element concentrations, respectively. Rb, Sr, Y, Zr, Nb, Hf, Ta, Th, U,
153 and REE analyses were carried out at the Department of Physics and Earth Sciences of the
154 University of Ferrara by means of a Thermo Series X inductively coupled plasma-mass
155 spectrometer (ICP-MS). Precision and accuracy were better than 10% for all elements, well

above the detection limit. Mineral phase major element chemistry was determined by using a CAMECA SX100 electron microprobe equipped with four WD and one ED spectrometers hosted at the Department of Lithospheric Research of the University of Wien. The operating conditions were as follows: 15 kV accelerating voltage, 20 nA beam current, and 20 s counting time on peak position. For feldspars, a 5 μm defocused beam and 10 s counting time on peak position for Na and K were used. Natural and synthetic standards were used for calibration, and PAP corrections were applied to the intensity data (Pouchou and Pichoir, 1991). Trace element concentrations of clinopyroxene were measured at the CNR - Istituto di Georisorse of Pavia by laser ablation microprobe-inductively coupled plasma-mass spectrometry (LAM-ICP-MS) following the protocols described by Tiepolo et al. (2003). NIST 610 and NIST 612 standard glasses were used to calibrate relative element sensitivity. Precision and accuracy for trace element analyses were assessed by standard sample BCR-2 (reference values from USGS Geochemical Reference Materials Database). Each analysis was corrected with internal standards using CaO. The detection limit, function of the ablation volume and counting time were calculated for each analysis. Since ablation volume greatly depends on laser type and sample (matrix), the detection limit decreased with decreasing spot size, beam power and cell gas flow. A 40-100 μm beam diameter and 20 μm/s scanning rate were used. The theoretical detection limit ranges from 10 to 20 ppb for REE, Ba, Th, U, Zr and are about 2 ppm for Ti. Whole-rock $^{87}Sr/^{86}Sr$ and $^{143}Nd/^{144}Nd$ analyses were made at the Scottish Universities Environmental Research Centre (SUERC) by thermal ionization mass spectrometry (TIMS) following procedures described by Casetta et al. (2018a). Eight measurements of SRM-987 and twelve of JNdi-1 made during the course of this analytical programme yielded mean values of 0.710244±0.000016 for $^{87}Sr/^{86}Sr$ and 0.512079±0.000018 (2 SD) for $^{143}Nd/^{144}Nd$, consistent with the consensus values of ~0.71025 and ~0.51210.

4. Petrography and mineral chemistry

Lava flows with trachybasaltic to trachyandesitic composition crop out in thick sequences emplaced over the Permo-Triassic volcano-sedimentary basement, and/or in direct contact with the coeval plutonic counterparts. Multiple dykes, ranging in thickness from 10-20 cm up to 1-2 m, cut both the basement and the volcano-plutonic bodies (Fig. 1). The crosscutting relationships between the dykes and the plutonic bodies have been used to reconstruct the temporal evolution of the multi-pulse Predazzo Intrusive Complex, which is composed of SiO_2-saturated (SS) to SiO_2-undersaturated (SU) batches (Casetta et al., 2018b). Geochemical and petrographic data (see below) support the discrimination between the two SS and SU suites for the dykes studied in the present work, which mirror the geochemical features of the plutonic rocks. They include hypersthene- to nepheline-normative trachybasalts, differentiating towards quartz- and nepheline-normative trachytes, respectively. All lavas, on the other hand, are SiO_2-saturated, highlighting how the occurrence of SU products was volumetrically limited.

4.1. Lava flows

The texture of the SS trachybasaltic to trachyandesitic lavas is generally porphyritic to glomeroporphyritic, with Porphyricity Index (P.I.) ranging from 5-10 up to 55-60%; these values suggest near hypabyssal conditions of the last stages of their crystallization (Fig. 2). The main phenocrysts are clinopyroxene (up to 3 mm), plagioclase (200 μm-2 mm) and spinel (50-500 μm), together with some rare olivine (up to 1 mm), often altered in iddingsite or serpentine, in the least differentiated samples (see Supplementary Material). Clinopyroxene ranges from diopside to augite (Morimoto, 1988), with Mg# [calculated as $Mg/(Mg+Fe_{TOT})$ mol%] and TiO_2 contents of 70.0-74.1 and 0.5-1.3 wt%, respectively (Fig. 3). Its Al_2O_3 content varies between 2.5 and 4.7 wt%, whereas Cr_2O_3 is always < 0.1 wt%. Occasionally, glomerophyric aggregates of clinopyroxene + spinel are observed. Spinel ranges in composition from magnetite to Ti-magnetite (TiO_2 = 0.1-17.4 wt%). Plagioclase, ranging in composition from bytownitic to labradoritic (An_{58-87}), is often sericitized in the less differentiated rocks, while it is quite fresh

208 in the trachyandesites. The groundmass of all lavas ranges from microcrystalline to
209 hypohyaline, constituted by the same mineral assemblage as the phenocrysts. Groundmass
210 plagioclase in the trachyandesitic lavas has andesinic composition (An_{37-44}).
211
212 ***4.2. Dykes***
213 The P.I. of the trachybasaltic to trachyandesitic dykes varies from 5-10% up to 50-55%. SS
214 trachybasaltic to trachyandesites have paragenesis and texture comparable to those of the lavas,
215 except for the groudmnass, which in some cases has coarser grain size and hosts some K-
216 feldspar crystals (Or_{79-90}). Plagioclase ranges in composition from bytownitic to labradoritic,
217 spinel is magnetite to Ti-magnetite, and clinopyroxene is similar in composition to the
218 phenocrysts in the SS lavas (Fig. 3) (see Supplementary Material).
219 Some trachybasaltic dykes, cropping out in proximity of the Latemar area (Fig. 1), have the
220 most primitive composition, and likely belong to the SU suite. They are constituted by
221 microcrystalline to hypohyaline groundmass, and clinopyroxene (400 μm-2 mm), plagioclase
222 (100-400 μm) and spinel (<200 μm) phenocrysts, together with fresh, zoned olivine phenocrysts
223 and xenocrysts (500 μm-2 mm; Fo_{85-92} cores to Fo_{78-81} rims, at NiO 0.07-0.15 wt%; Fig. 2). In
224 these dykes, clinopyroxene phenocrysts are Al-Cr-diopsides, with Mg# between 78.1 and 85.0,
225 TiO_2 contents up to 2.0 wt% and Cr_2O_3 contentrations ranging from 0.1 to 1.0 wt% (Fig. 3).
226 Some phenocrysts exhibit compositional zoning, with Cr-diopsidic cores (Mg# up to 88.4; TiO_2
227 = 0.2 wt%; Cr_2O_3 = 0.5 wt%) graded in diopsidic-augitic rims (Mg# down to 67.6; TiO_2 up to
228 1.0 wt%; Cr_2O_3 ~0.02 wt%). Throughout SU dykes, plagioclase phenocrysts range in
229 composition from bytownite to labradorite, whereas spinel encompass the magnetite to Ti-
230 magnetite compositional range. Spinel composition is different, however, in the least
231 differentiated SU trachybasaltic dyke, and ranges from Ti-magnetite to Cr-spinel (TiO_2 = 0.8-
232 16.9 wt%; Cr_2O_3 = 4.0-28.3 wt%). Groundmass K-feldspar ranges in composition from Or_{79} to
233 Or_{90}.

234 The trachytic dykes, distinguishable in the field by their bright pink to grey (SS quartz-
235 trachytes) or light pink to greenish (SU nepheline-trachytes) colours, have low P.I. (usually
236 <25%). Quartz-trachytes are mainly constituted by K-feldspar (300 μm-4 mm), plagioclase (up
237 to 7 mm) and spinel (<200 μm) phenocrysts in a micro- to cryptocrystalline groundmass made
238 by apatite, feldspars, biotite, quartz and Fe-Ti oxides. Nepheline-trachytes are usually highly
239 altered, and composed of K-feldspar (1-5 mm), plagioclase (up to 1 mm), and rare nepheline
240 phenocrysts in a cryptocrystalline to hypohyaline groundmass. Plagioclase phenocrysts and
241 groundmass crystals in SS-SU trachytes have large compositional variations, ranging from
242 labradorite to albite. K-feldspar is quite homogeneous, ranging from Or_{92} to Or_{99}.
243 Overall, the composition of clinopyroxene phenocrysts is the best proxy for discriminating
244 between the SS and SU suites: clinopyroxene in SS rocks is generally more depleted in TiO_2
245 with respect to those in SU samples, at comparable Mg# (Fig. 3). Such a feature further
246 evidences the more pronounced "alkaline" character of SU samples with respect to the SS ones,
247 fostering a discrimination between the two suites.
248
249 ***4.3. Ultramafic cumulates***
250 In the Latemar area, some SU trachybasaltic dykes contain ultramafic xenoliths (Figg. 1-2). The
251 least altered clinopyroxenites have cumulitic texture, with small (200-300 μm) to medium-sized
252 (2-3 mm) fresh clinopyroxene crystals in contact by means of triple junctions, and sometimes
253 enclosing small olivine grains (Fig 2). Clinopyroxene is diopside (Mg# = 85.5-87.6; Wo = 47-
254 48), with TiO_2 and Cr_2O_3 contents of ~0.2 wt% and 0.1-0.3 wt%, respectively (Supplementary
255 Material). At the edges of the xenolith, the contact with the host SU trachybasalt induced
256 marked TiO_2 (up to 2.3 wt%) and Cr_2O_3 (up to 1.2 wt%) enrichments, coupled with a general
257 decrease in the Mg# (from 84.0 down to 62.5). Beside these contact areas, clinopyroxene show
258 compositional analogies with the phenocrysts of the SS suites (Fig. 3). In chondrite-normalized
259 (Sun and McDonough, 1989) incompatible element patterns, these clinopyroxene have Rb-Ba

and Nb-Ta depletions, as well as marked Zr-Hf and Ti negative anomalies. Their REE patterns have the convex-upward shape typical of alkaline magmas, with $(La/Yb)_N$ values of 1.91-2.00 (Fig. 3). Although preserving the significant HFSE paucity, clinopyroxene grains in proximity of the contact with the host basalt are significantly REE-enriched, and have $(La/Yb)_N$ values of ~1.6 (Fig. 3).

5. Whole-rock geochemistry

5.1. Major and trace element chemistry

Lavas and dykes belong to both the alkaline and transitional series with K-affinity (Fig. 4). On the Total Alkali vs. Silica (TAS) diagram (Fig. 4), lavas plot between the basaltic and the trachyandesitic fields (SiO_2 = 49.2-59.9 wt%; Na_2O+K_2O = 3.1-8.5 wt%), whereas dykes show wider compositional variations, from basaltic to trachytic and phonolitic (SiO_2 = 48.1-63.7 wt%; Na_2O+K_2O = 3.4-12.2 wt%) (Fig. 4; Table 1). The Mg# [calculated as MgO/(MgO+FeO) mol%, considering a Fe_2O_3/FeO ratio of 0.15, in agreement with fO_2 around +1 ΔFMQ (Kress and Carmichael, 1991; Casetta et al., 2018a)] of the lavas ranges from 64.3 in trachybasaltic samples down to 41.5 in trachyandesites, whereas dykes have Mg# of 65.4 (trachybasalts) to 23.7 (trachytes). The TiO_2 and FeO_{TOT} contents, as well as the CaO/Al_2O_3 ratio of the samples are inversely correlated with the silica content, and decrease from 1.5 to 0.2 wt%, from 10.5 to 2.0 wt% and from 0.78 to 0.03, respectively (Fig. 4). Similarly, Ni decreases from 89 to 1 ppm, while Zr, Nb and Rb concentrations increase from 77 to 779 ppm, from 5 to 51 ppm and from 12 to 344 ppm, respectively, with increasing SiO_2 (Fig. 4). As for the corresponding intrusive suites (Casetta et al., 2018a; 2018b), SU and SS rocks can be easily discriminated by their FeO contents, CaO/Al_2O_3 and Na_2O/K_2O ratios, as well as by their Rb, Zr and Nb concentrations at comparable silica content (Fig. 4).

In the Primitive Mantle- (PM; Sun and McDonough, 1989) normalized incompatible element diagram, all lavas and dykes are enriched in LILE, Th-U and LREE, and display the Nb-Ta and

Ti negative anomalies typical of magmatic suites generated by subduction-modified mantle source (Fig. 5). Moving from trachybasaltic to trachytes, the incompatible element patterns are increasingly enriched in LILE and depleted in Ti. All samples have flat Middle (M-) to Heavy (H-) REE profiles in chondrite-normalized (Sun and McDonough, 1989) diagrams, and moderate enrichment in LREE, with $(La/Yb)_N$ values comprised between 8.5 and 9.5 for the least differentiated rocks of both suites (Fig. 5). Despite the similar incompatible element concentrations with respect to the most primitive SS lavas and dykes, SU trachybasalts have slightly higher Zr-Hf abundances, and less pronounced Nb-Ta-Ti anomalies. Significant differences can be envisaged by comparing the most differentiated trachytic products of the two suites: SU trachytes have extremely higher Th-U, Zr and LREE concentrations with respect to SS ones, this latter parameter resulting in a marked difference in their $(La/Yb)_N$ ratios (Fig. 5; Table 1). On the Th_N vs. Nb_N tectonic discrimination diagram (Fig. 6a), the SS/SU volcanic series fall within the calc-alkaline, (i.e. orogenic) field. Their HFSE distribution is well consistent with magmatic suites from active continental margins, as also testified by the distribution of the least differentiated SS-SU rocks on the Th-Hf-Ta diagram (Fig. 6c). In both diagrams, the marked difference between Mid-Triassic SS/SU rocks and Late Triassic lamprophyres from the same area (Casetta et al., 2019) supports the hypothesis that different mantle sources were activated within a period of ~20 Ma to generate the distinct magmatic events. This feature is also highlighted by the Nb/La vs. La/Yb ratios of the least differentiated SS/SU rocks (Fig. 6b), which suggest that the contribution of lithospheric mantle in their genesis was more pronounced than for lamprophyres, which bear witness of a marked asthenospheric involvement.

5.2. $^{87}Sr/^{86}Sr$ and $^{143}Nd/^{144}Nd$

Whole-rock $^{87}Sr/^{86}Sr$ and $^{143}Nd/^{144}Nd$ isotopic ratios were measured on representative samples of lavas and dykes from both the SS and SU suites (Table 1). Initial isotopic ratios, respectively

named $^{87}Sr/^{86}Sr_i$ and $^{143}Nd/^{144}Nd_i$, were corrected to an age of 238 Ma, in accordance with the recently published U-Pb datings (from 238.19±0.05 to 237.58±0.04 Ma; Storck et al., 2020). Lavas and dykes from the SS suite have $^{87}Sr/^{86}Sr_i$ values ranging from 0.7043 to 0.7057, and $^{143}Nd/^{144}Nd_i$ from 0.51219 to 0.51235 (Fig. 7). Dykes belonging to the SU suite are characterized by slightly higher $^{87}Sr/^{86}Sr_i$ (0.7055-0.7058) with respect to SS rocks, at $^{143}Nd/^{144}Nd_i$ of 0.51226-0.51232. On the whole, Sr-Nd isotopic data for the SS and SU lavas and dykes are similar to those of the corresponding intrusive rocks, lying in proximity of the enriched mantle (EM I) end-member, in line with most of the Southern Alps Mid-Triassic magmatic rocks (Fig. 7; Lustrino et al., 2019). They are also well distinct from the Late Triassic lamprophyres, which plot close to the depleted MORB mantle (DMM) end-member (Fig. 7; Workman and Hart, 2005). The only available analysis for cumulitic clinopyroxenite xenoliths yields an $^{87}Sr/^{86}Sr_i$ value of 0.7044, i.e. similar to those of the SS rocks, but slightly lower with respect to the initial Sr ratios typical of SU dykes.

6. The primary shoshonitic magmas and their SCLM source

6.1. Reconstruction of primary shoshonitic melts

The variable extent of differentiation that affected the Mid-Triassic shoshonitic rocks makes it difficult to understand the compositional features of the primary melts, and from there to understand the nature of the underlying SCLM. The least evolved lavas and dykes have Mg# always <65, and are often characterized by moderate to high crystal cargoes (P.I. up to 50-55), which result in "doped" bulk rock analyses, where the high Mg# and the low REE abundances are function of the hypabyssal nature of the rocks rather than of their primitivity. No melt inclusions where found in the early-forming phases (olivine or clinopyroxene), being the composition of the most Mg-rich crystals inside lavas, dykes and cumulitic xenoliths (Fig. 3) the only petrological evidence for the existence of primitive melts. For these reasons, the most Mg-rich and least porphyritic dykes from the two magmatic suites (SS-SU) were chosen and

traced back to the ideal condition of equilibrium with a fertile mantle assemblage, in line with what proposed by Casetta et al. (2020) for Mt. Etna magmas. Olivine and clinopyroxene plus small amounts of Cr-bearing spinel were re-added to the melt in a backward fractionation process, being aware of respecting the Fe-Mg equilibrium conditions between the progressively reconstructed melt and each added mineral phases (i.e. $^{Ol\text{-}Melt}Kd_{Fe\text{-}Mg}$ = 0.27-0.33 and $^{Cpx\text{-}Melt}Kd_{Fe\text{-}Mg}$ = 0.24-0.30; Roeder and Emslie, 1970; Putirka, 2008). The occurrence of high-Fo olivine xenocrysts and olivine inclusions in cumulitic clinopyroxene suggests that olivine dominated the earlier crystallization stages, probably in a restricted *T-P* interval, followed in a rapid sequence by clinopyroxene in the possible liquid line of descent of these magmas. Therefore, olivine + clinopyroxene (diopside-augite) assemblages, together with small amounts of Cr-bearing spinel, were progressively re-added to the chosen starting SS and SU rocks until their major element composition resulted in equilibrium with a fertile mantle source (i.e. Mg# 68-70, in equilibrium with a $Fo_{88\text{-}90}$ olivine; see McDonough, 1990). The trace element composition of the ideal primitive SS and SU melts was modelled by means of the Rayleigh fractionation equation (Shaw, 1979), following Casetta et al. (2020). The adopted mineral/melt trace element partition coefficients are listed in the Supplementary Materials. The primary transitional to alkali basaltic SS and SU melts were obtained after 10.5-11.4% backward fractionation of olivine (6.6-6.9 vol.%), clinopyroxene (2.4-3.0 vol%) and spinel (1.5 vol.%) (Table 2). The modelled primitive melts have Mg# ~70 and preserve the above-mentioned differences between the SS and SU suites, in terms of both major and trace element features (Fig. 4). Their PM-normalized incompatible element patterns are characterized by LILE-enrichment as well as Nb-Ta-Ti negative anomalies, these latter less marked in the primitive SU melt, which preserve the slightly higher Zr-Hf abundance with respect to the SS one (Fig. 5). When compared to the Late Triassic lamprophyres, SS and SU rocks can be easily discriminated on the basis of their HFSE abundances (Fig. 5).

364 ***6.2. The composition of the mantle source***

365 The shoshonitic affinity and incompatible element distribution of the studied magmas indicate
366 their derivation from an enriched SCLM source modified by subduction-related components.
367 In fact, Sr-Nd, Pb and Hf isotopic signatures point towards an enriched mantle-derived
368 fingerprint, and rule out the effect of large (>10%) crustal assimilation during the peak of
369 effusive magmatism at 238 Ma (Casetta et al., 2018a; De Min et al., 2020; Storck et al., 2020).
370 Several authors hypothesized a decoupling between the timing of the shoshonitic magmatism
371 and the metasomatism of the lithospheric mantle source, relating this latter process to the
372 Variscan subduction (Bonadiman et al., 1994; Lustrino et al., 2019). Direct evidence of the
373 impact of the Variscan subduction on the Southern Alps SCLM is visible in the Ulten and Finero
374 peridotitic massifs, where modal (i.e. presence of amphibole, phlogopite, Cl-rich apatite) and/or
375 cryptic subduction-related metasomatism is documented (e.g., Zanetti et al., 1999; 2016;
376 Tumiati et al., 2003; Ionov et al., 2017; Tommasi et al., 2017).

377 To simulate the slab-derived modification of the Southern Alps SCLM, Sr-Nd isotopic mixing
378 models (Faure, 1986; see also Melchiorre et al., 2020) between DMM and selected subduction-
379 related components were performed. The average composition of the global subducting
380 sediments (GLOSS/GLOSS-II; Plank, 2014) and the average composition of the Southern Alps
381 crust (Voshage et al., 1990) were chosen to represent possible end-members of subducting
382 crustal components, for modelling the Sr-Nd isotopic variability caused by slab-derived
383 influxes (see Kessel et al., 2005; Plank, 2014). The SS rocks lie on a mixing trend between
384 DMM and GLOSS-II, whereas the relative Sr-Nd isotopic enrichment of SU magmas
385 approaches the mixing curve between DMM and GLOSS, confirming that two different mantle
386 sources are associated to the genesis of SS and SU magmas. By contrast, the Finero
387 amphibole+phlogopite-bearing peridotite samples plot towards the GLOSS-II end-member,
388 resulting slightly more enriched in radiogenic Sr with respect to SS magmas (Fig. 7). The Ulten
389 peridotites span a large Sr-Nd isotopic range, as result of complex interactions between mantle

and metasomatising fluids with crustal signature (Fig. 7; see Tumiati et al., 2003). Metasomatic amphibole and phlogopite in the Finero phlogopite peridotite, recording post-Variscan ages as old as 310 Ma (Zanetti et al., 2016; Malitch et al., 2017, and references therein), mostly plot along the mixing trend between DMM and the average crust (Fig. 7), enhancing the role played by subduction-related melts/fluids in metasomatising the Southern Alps SCLM prior to 290 Ma (Hartmann and Wedepohl, 1993; Zanetti et al., 1999; 2016; Selverstone and Sharp, 2011; Giovanardi et al., 2020). Following the Sr-Nd isotopic mixing models, the ideal trace element composition of the enriched SCLM domains that generated the SS/SU primary melts has been firstly approached by mixing DMM with 4% GLOSS-II (SS magmas) and 2% GLOSS (SU magmas) components. The inferred mantle source of SS magmas has LILE-enrichment, Nb-Ta-Ti negative troughs, slight LREE-enrichment and PM-like MREE-HREE contents (Fig. 8). The calculated mantle source of SU magmas is relatively depleted in all trace elements with respect to the SS one, being typified by PM-like LREE concentrations and DMM-like MREE-HREE profiles (Fig. 8).

Subsequently, the mineral phases of highly fertile composition from the Southern Alps peridotitic massifs (Mazzucchelli et al., 2010; Giovanardi et al., 2020) were used to model the trace element content and modal composition of the ideal "SS" and "SU" sources *via* mass balance calculations. Results showed that the trace element concentrations of the ideal "SS" and "SU" sources are matched by considering two amphibole+phlogopite-bearing spinel-lherzolites with the following modal compositions: 55.4% olivine + 23.0% orthopyroxene + 17.7% clinopyroxene + 1.1% spinel + 2.0% amphibole + 0.8% phlogopite (SS source); 57.5% olivine + 24.3% orthopyroxene + 15.1% clinopyroxene + 1.1% spinel + 1.4% amphibole + 0.6% phlogopite (SU source) (Table 3). It should be highlighted that all the considered phases belong to the Finero phlogopite peridotite, except clinopyroxene, which is from the Baldissero peridotite. Clinopyroxene in the Finero phlogopite peridotite in fact is highly depleted, recording up to ~20% melt extraction (Coltorti and Siena, 1984; Hartmann and Wedepohl,

1993), being thus unsuitable for simulating an enriched mantle source. By considering the maximum H_2O contents measured in the mineral phases of the Finero peridotite (3.2 ppm olivine; 111 ppm orthopyroxene; 267 ppm clinopyroxene; 1.93 wt% amphibole; 4.3 wt% phlogopite; Tommasi et al., 2017), the amounts of H_2O retained in the modelled SS and SU mantle sources would result of 784 and 598 ppm, respectively (Table 3). These values are well within the range proposed for other worldwide SCLM domains, such as the Subei Basin in China (328-1440 ppm H_2O; Hao et al., 2019) or the Norther Victoria Land in Antarctica (910-1486 ppm H_2O; Giacomoni et al., 2020). In line with the trace element and Sr-Nd isotopes mixing results, the compositional discrimination between the modelled SS and SU sources is mirrored by different incompatible elements and H_2O concentrations, in turn related to the lower modal amounts of clinopyroxene, amphibole and phlogopite (Fig. 8).

7. The genesis of shoshonitic magmatism

7.1. Mantle source melting model

The partial melting conditions of the mantle sources required to produce the primary SS and SU transitional to alkali basaltic melts were simulated by using the mineral phase modal proportions and the eutectic composition of the peridotitic systems as function of the degree of partial melting (see Casetta et al., 2020). A "melting+recrystallization" mass balance model enabled us to simulate the contribution of the fusible components (e.g., TiO_2, Al_2O_3 and alkalis) from each mineral phase of the lherzolitic source, and then reproduce the major element composition of the produced magmas. In this process, the contribution during melting of each phase with fertile composition is counterbalanced by recrystallization of a restitic residuum (e.g., melting of Al-rich clinopyroxene + recrystallization of Al-poor clinopyroxene), in accordance with the conditions of melting of a amphibole+phlogopite-bearing lherzolite in the spinel stability field (Gaetani and Grove, 1998; Conceição and Green, 2004; Liu et al., 2006;

Condamine and Médard, 2014). The relative contribution of each mineral phase at the eutectic was evaluated, for major elements (oxide, wt%) by least square method, following the equation:

$$S = \sum_{i=1}^{n} r_i^2 \, .$$

Here, the optimal parameter S is fitted by minimizing the sum of squared residuals r^2 between the predicted values for each oxide "i" (e.g., SiO_2 wt% of the primitive melt) and the values calculated from the melting model (e.g., SiO_2 wt% resulting from the "melting+recrystallization" process). For our purposes, the model was considered accurate when S <1, i. e. when the difference between modelled and calculated parameters, expressed as oxides wt%, is well within the analytical errors (i.e. XRF and/or EPMA determinations). The partial melting degree (F) associated to the production of primitive melts was then calculated as the difference between the melted fertile assemblage and the recrystallized restitic residuum, checking the consistency with the experimental data on genesis of shoshonitic melts (e.g., Conceição and Green, 2004). Once fixed the mineral phase proportions required to produce the primary SS/SU magmas at the eutectic, the non-modal batch melting equation of Shaw (1979) was applied to model their trace element distribution. In this equation, expressed as:

$$C_L = \frac{C_0}{[D+F\times(1-P)]} \, ,$$

C_L represents the concentration of each trace element in the primary melt, C_0 its concentration in the modelled source, D its partition coefficients weighted for the modal composition of the source and P the partition coefficients weighted for the eutectic mineral proportions (see Table 2 and Supplementary Material for the partition coefficients and mineral melting proportions). The application of this equation to elements with highly incompatible behaviour, i.e. with $D \rightarrow 0$ and $P \rightarrow 0$, approximated by the ratio:

$$F = \frac{C_0}{C_L} \, ,$$

was also used throughout the calculations to check the consistency of the partial melting degrees.

7.2. Partial melting conditions and role of H_2O

The partial melting models suggest that 7% partial melting of a fertile spinel-lherzolite bearing small proportions of amphibole (1.98%) and phlogopite (0.76%) can produce the major/trace element content of primary SS transitional basalt. Hydrous phases were totally consumed during this melting stage, significantly contributing to the eutectic of the system (Table 4). A negligible contribution of spinel accompanied by positive melting proportions of orthopyroxene, clinopyroxene and by dominant recrystallization of olivine, is also required to account for the major/trace element distribution of primary SS melts. On the other hand, the production of the SU primary alkali basalt can be explained by 5% partial melting of a spinel-lherzolite with slightly lower abundances of hydrous phases (1.36% amphibole + 0.62% phlogopite). Again, hydrous phases were completely consumed, together with significant proportions of orthopyroxene and clinopyroxene. Using experimental estimations of mineral-melt water partitioning during peridotite melting, the estimated H_2O amounts of the produced primary melts are in the range of 1.06-1.12 wt% (Table 4; Supplementary Material). In terms of trace elements, the predicted and calculated SS/SU melts are very close, especially the LILE and REE (Fig. 9). In both models, the main discrepancies are related to U, Zr-Hf and Sr, whose concentrations in the sources resulted too low to match those of the primary melts (see discussion below).

7.3. Peridotite melting and mantle source depth

Conceição and Green (2004) showed that decompression melting of a metasomatised spinel-peridotite bearing small amounts amphibole and phlogopite can produce shoshonitic magmas at ~5% partial melting, T = 1075°C and P = 1.0 GPa, by exhausting hydrous phases very close

491 to the solidus. Consistent with their findings, our model shows that 5-7% melting of an
492 amphibole+phlogopite-bearing spinel lherzolite can reproduce the composition of the primary
493 SS/SU melts, requiring the complete disappearance of both amphibole and phlogopite.
494 During the two melting stages, the contribution of the pyroxenes was opposite. Indeed, while
495 the SS melting stage was characterized by an orthopyroxene-dominated eutectic, in the SU
496 melting stage the maximum contribution at the eutectic was given by clinopyroxene (Table 4).
497 This behaviour can be explained by the role played by volatiles (H_2O, CO_2) and alkalis during
498 partial melting. Experimental studies showed that the amount of clinopyroxene and
499 orthopyroxene consumed during melting of spinel lherzolites at 1.1-1.2 GPa are negatively and
500 positively correlated to the amount of H_2O in the system, respectively (Gaetani and Grove,
501 1998; Condamine and Médard, 2014). Moreover, Liu et al. (2006) found that the effect of H_2O
502 is somewhat similar to that of K_2O, so that increasing the concentration of these elements in the
503 peridotitic source results in the genesis of SiO_2-saturated (to oversaturated) melts. Conversely,
504 decreasing H_2O and/or increasing Na_2O in the source system leads to the production of
505 nepheline-normative liquids (Liu et al., 2006). Accordingly, the slightly different H_2O contents
506 of the SS and SU sources are associated to the genesis of hypersthene- and nepheline-normative
507 melts, respectively.
508 According to Selverstone and Sharp (2011) results, the Finero amphibole-phlogopite peridotite
509 equilibrated at *P* of 1.2-1.6 GPa. These values are consistent with the experimental works on
510 the genesis of shoshonitic melts from peridotitic sources (e.g., Conceição and Green, 2004) and
511 with the experimental studies on amphibole/phlogopite stability in the SCLM (Condamine and
512 Médard, 2014; Mandler and Grove, 2016). In this framework, it is likely that the transitional to
513 alkali basaltic SS/SU melts were generated was located at 40-60 km of depth, i.e. well above
514 the spinel-garnet transition in SCLM domains (2-3 GPa, i.e. 60-90 km; Falloon and Green,
515 1988). This melting depth is consistent with the equilibration depth calculated by Carraro and
516 Visonà (2003) for the spinel-lherzolitic xenoliths sampled along the same SCLM column (i.e.

517 ~45 km), and quite shallower than the one from which alkaline lamprophyres were generated
518 during the subsequent Late Triassic cycle (70-80 km; Casetta et al., 2019).
519
520 **8. The ascent and emplacement of the Middle Triassic melts**
521 ***8.1. Equilibrium conditions and adopted thermobarometric/hygrometric models***
522 The *T*-*P*-H_2O paths followed by SS and SU melts in the interval comprised between segregation
523 from the mantle source and their emplacement/differentiation in shallow crust were tracked by
524 means of thermobarometric and hygrometric equations based on olivine- and clinopyroxene-
525 melt equilibria. To reconstruct the *T* conditions of crystallization of the least differentiated SU
526 magmas, the olivine- and clinopyroxene-melt thermometers of Putirka (2008; Equations 22 and
527 33) were applied to the phenocrysts yielding equilibrium with the whole-rock composition of
528 the host dykes (i.e. $^{Ol\text{-}Melt}Kd_{Fe\text{-}Mg}$ = 0.27-0.33 and $^{Cpx\text{-}Melt}Kd_{Fe\text{-}Mg}$ = 0.24-0.30; Fig. 10). Due to
529 the generally low crystal cargo of the SU trachybasaltic dyke (P.I. down to 5-10%; Table 1), its
530 whole-rock compositions was considered a good approximation of a melt composition. The
531 pressures of clinopyroxene crystallization were calculated by means of the Putirka (2008,
532 Equation 32b) H_2O-dependent barometer, in turn derived from the Putirka et al. (1996, Equation
533 T1) thermometer. Because of the sensitivity of the chosen thermobarometers to the H_2O content
534 of the melt, multiple calculations were performed using as input variable amounts of H_2O (from
535 1 to 5 wt%). These H_2O-dependent equations were then iterated with the *T*-*P*-dependant
536 clinopyroxene-based hygrometer of Perinelli et al. (2016) until matching results were obtained,
537 in a process that enable to skip circular assumptions of the *T*-*P*-H_2O conditions of the
538 crystallizing melts (see Casetta et al., 2018a; Lanzafame et al., 2020).
539 Due to the absence of unaltered olivine phenocrysts, the primary *T*-*P*-H_2O conditions of
540 crystallization of SS melts were modelled by applying thermobarometric and hygrometric
541 equations to clinopyroxene in early-derived clinopyroxenitic cumulates. Accordingly,
542 clinopyroxene grains inside clinopyroxenitic xenolith were traced back to the equilibrium

543 conditions with the least differentiated SS trachybasaltic dyke in terms of both major (Fig. 10a)
544 and trace elements (Fig. 10b; see Supplementary Material for the adopted mineral-melt partition
545 coefficients for trace elements). The most Mg-poor clinopyroxenes in trachybasaltic lavas
546 resulted in clear disequilibrium with their host rock (Fig. 10), likely because the high P.I. of the
547 studied lavas, crystallized in almost hypabyssal conditions, make them far from resembling a
548 melt in terms of whole-rock composition. Therefore, these crystals were traced back to
549 equilibrium conditions (i.e. $^{Cpx\text{-}Melt}Kd_{Fe\text{-}Mg}$ = 0.24-0.30; Putirka, 2008) with less porphyritic
550 trachybasaltic and trachyandesitic rocks belonging to the same magmatic suite (see also Casetta
551 et al., 2018a). Afterwards, the chosen clinopyroxene-melt thermobarometers and hygrometers
552 (Putirka, 2008; Perinelli et al., 2016) were iteratively applied to determine the *T*-*P*-H_2O space
553 of clinopyroxene crystallization. Unfortunately, no reliable *P*-H_2O results were obtained by the
554 iterative procedures for the clinopyroxene crystals inside clinopyroxenitic xenoliths. Therefore,
555 to obtain a rough estimate of their crystallization *P*, the Putirka et al. (2003) H_2O-independent
556 barometer was used. Further details, together with a complete list of the obtained results and of
557 the errors associated to each adopted equation are listed in Table 5.
558
559 ***8.2. T-P-H_2O paths***
560 Thermometric models showed that the phenocrysts of olivine (Fo_{85}) and clinopyroxene ($Mg\#_{Cpx}$
561 85) in equilibrium with the SU trachybasaltic dyke ($Mg\#_{Liq}$ 64) record the most congruent
562 crystallization *T* (from 1195 to 1204-1207 °C), by considering a H_2O content in the melt of 1.5-
563 1.9 wt%. The corresponding crystallization *P* obtained from the clinopyroxene-melt barometer
564 is ~830 MPa (Fig. 10). The deepest conditions of crystallization of SS magmas (*P* = 570-710
565 MPa) are from clinopyroxene grains inside cumulitic xenoliths ($Mg\#_{Cpx}$ 86-88) in equilibrium
566 with the SS trachybasaltic dyke ($Mg\#_{Liq}$ 65), at *T* between 1100 and 1128 °C (Fig. 10). The
567 most Mg-poor clinopyroxene phenocrysts ($Mg\#_{Cpx}$ 70-83) analysed in SS trachybasaltic to
568 trachyandesitic lavas and dykes (equilibrium melts = $Mg\#_{Liq}$ 41-53) record shallower

569 conditions. Their crystallization occurred along a polybaric path at *P* comprised between 470
570 and 230-170 MPa, until the onset of a nearly isobaric cooling regime took place at *P* of 50-170
571 MPa (Fig. 10). Although plausible and in line with previous estimates for the same magmatic
572 suite (e.g., Casetta et al., 2018a; De Min et al., 2020), these *T-P* results have to be considered
573 together with the associated errors (i.e. ±29-42°C; ±170-260 MPa; Table 5).
574
575 **9. Discussion**
576 ***9.1. The Southern Alps SCLM and the genesis of shoshonitic melts***
577 A possible relationship between the metasomatized orogenic peridotites and the Mid-Triassic
578 orogenic-like magmatism in the Southern Alps has been often hypothesized (Zanetti et al.,
579 1999; 2013; Mazzucchelli et al., 2010; De Min et al., 2020). As shown in Fig. 7, the shoshonitic
580 magmas of the Dolomites share a common enriched (EM I-like) Sr-Nd isotopic signature
581 (Bonadiman et al., 1994; Casetta et al., 2018a; Lustrino et al., 2019), mirroring the fingerprint
582 of the underlying mantle source. The existence of K-H_2O-rich mantle-derived melts in the
583 Southern Alps SCLM during Mid-Triassic is also supported by the intrusion of gabbroic dykes
584 with similar Sr-Nd isotopic signature to the SS/SU magmas inside the Finero peridotite
585 (Giovanardi et al., 2020). According to many authors, the slab-derived enrichment of the
586 Southern Alps SCLM has to be ascribed to the Variscan subduction (Bonadiman et al., 1994;
587 Lustrino et al., 2019), the effect of which are also preserved in the metasomatised Finero and
588 Ulten peridotites (Zanetti et al., 1999; Ionov et al., 2017; Giovanardi et al., 2020). In the Finero
589 peridotite, several generations of hydrous phases (amphibole and phlogopite) formed after
590 pervasive and prolounged metasomatism of depleted harzburgites (Voshage et al., 1987;
591 Hartmann and Wedepohl, 1993; Zanetti et al., 1999; 2013; 2016; Tommasi et al., 2017;
592 Giovanardi et al., 2020). The infiltration of slab-related metasomatic agents in the Finero main
593 peridotitic body is also suggested by the Nb-Ta-Ti negative anomalies and enrichment in
594 radiogenic Sr of amphibole grains, which lie on the mixing trend between DMM and the

595 average crustal (and/or GLOSS/GLOSS-II) components (Fig. 7; see also Giovanardi et al.,
596 2020). Although partially overprinted by the complex *T-P-t* trajectories followed from
597 depletion to the subsequent Palaeozoic metasomatism and the Mesozoic (~180 Ma) exhumation
598 at shallower levels (Hartmann and Wedepohl, 1993; Zanetti et al., 2016; Langone et al., 2017),
599 the Finero peridotite is the best approximation of the Southern Alps SCLM during
600 MiddleTriassic, i.e. at the time of the shoshonitic magmatism. Accordingly, our models enabled
601 us to set out that an assemblage composed of phases with most fertile composition from the
602 Finero (and Baldissero) peridotite is able to approach, in terms of major/trace elements, a bulk-
603 rock source composition similar to that resulting from a mixing between DMM (98-96%) and
604 GLOSS/GLOSS-II (2-4%) components (Fig. 9; Table 3). Besides confirming the role played
605 by subductive crustal components in the modification of the Southern Alps SCLM, the
606 modelled fertile mantle source perfectly encompasses the Sr-Nd isotopic variations of the Mid-
607 Triassic shoshonitic magmas (Fig. 7; Table 1). The modelled sources are consistently able to
608 account for the major/trace element composition of the primary SS/SU magmas at 5-7% partial
609 melting. These melting degrees are higher than those hypothesized by Lustrino et al. (2019),
610 who suggested that a supra-subductive peridotite interacting with slab-derived components is
611 able to generate the Mid-Triassic shoshonitic magmatism at 2% slab + 1.1% peridotite melting.
612 According to these authors, although reliable in terms of geodynamic interpretation, such a
613 model is limited by the use of a non-primary target melts (Mg# 61), resulting in excessively
614 low degrees of partial melting.
615 The incompatible element patterns of the modelled SS/SU melts mirror those of the primary
616 magmas, except for some discrepancies in the Th-U, Sr and Zr-Hf distributions (Fig. 9), which
617 likely reflect the low concentrations of these elements in the modelled sources, i.e. in the
618 mineral phases in the Finero peridotite (see Giovanardi et al., 2020). The “ideal” mantles
619 resulting from the mixing between DMM and GLOSS/GLOSS-II components are enriched in
620 Th-U and Zr-Hf with respect to the modelled Finero-like sources (Fig. 9). The positive Sr spike

621 in the primary melts, a peculiar feature of magmas generated from subduction-modified sources
622 (Zheng, 2019), cannot be reproduced neither by the modelled sources nor by the "mixed"
623 DMM+GLOSS mantles. This discrepancy could be explained by the variable concentration of
624 Sr in worldwide sediments (see Plank, 2014) or, alternatively, by the extremely variable and *T*-
625 *P*-dependent mobility of Sr in metasomatic melts/fluids and/or supercritical fluids in
626 subduction-related settings (Kessel et al., 2005).
627
628 ***9.2. Ascent and emplacement of the Middle Triassic magmas***
629 The maximum *P* of crystallization of SS/SU magmas yielded by clinopyroxene-melt
630 barometers are comprised between 710 and 830 MPa (i.e. 24.5-28.6 km assuming a $\Delta P/\Delta z$ of
631 ~29 MPa/km; Fig. 10). During ascent, the crystallization processes continued in a polybaric
632 regime until 160-230 MPa, where the nearly isobaric cooling from *T* of 1060 °C down to *T*
633 <1000 °C reflects the formation, in a shallow crustal environment, of discrete magma batches,
634 dominated by the onset of fractional crystallization processes (Fig. 10). Evidence of the
635 progressive alkali- and H_2O-enrichment during the shallow evolution of the melts are widely
636 documented in the Predazzo and Mt. Monzoni plutons, which record emplacement *P* of 40-165
637 MPa (Bonadiman et al., 1994; Casetta et al., 2018a). The hygrometric results show that
638 clinopyroxene crystallization in SS and SU melts took place at progressively increasing H_2O
639 amounts, from 1.7 wt% in trachybasalts at 710-830 MPa up to 3.9 wt% in trachyandesites at
640 380 MPa (Fig. 10; Table 5). Such H_2O concentrations are not far from what expected if a
641 completely incompatible behaviour of H_2O is assumed during progressive differentiation of
642 mantle-derived transitional to alkali basaltic melts with ~1.1 wt% H_2O. At shallower *P*, volatiles
643 exsolution promoted crystallization of clinopyroxene, feldspar and Fe-Ti oxides, followed by
644 amphibole and phlogopite in the case of magmas differentiating and cooling in
645 hypabyssal/plutonic conditions (Fig. 10).
646

9.3. Geodynamic implications: a mantle perspective

Our study provides a robust link between the shoshonitic magmatism of the Dolomites and the metasomatised Finero peridotite, enabling speculation about the evolution of the Southern Alps SCLM. In fact, 7% partial melting of a Finero-like mantle containing ~800 ppm H_2O is able to generate primary transitional basaltic SS melts resembling those emplaced during the most productive phase of the Mid-Triassic (239-237 Ma) magmatism in the Dolomites. On the other hand, 5% partial melting of a slightly different SCLM domain (H_2O ~600 ppm) produced the SU primary alkali basaltic melts, which emplaced mostly in form of dykes and small intrusive bodies, for which no age data have been reported so far. The progressive depletion of the SCLM beneath the Southern Alps continued towards Late Triassic, when the asthenospheric influx related to the Alpine Tethys opening phase led to the production of alkaline lamprophyres with anorogenic signature at 219.22±0.73 Ma (Casetta et al., 2019). The extreme volatile-rich nature of lamprophyres can be ascribed to small degree partial melts (1-0-2.5%) of their amphibole-garnet-lherzolitic source (Casetta et al., 2019). Overall, the shifting from shoshonitic to alkaline magmatism recorded in the Dolomites is a very effective way to track progressive depletion, in terms of both major/trace elements and volatiles content, of the Southern Alps SCLM prior to the rifting phase connected to the Alpine Tethys opening.

On the other hand, the retention of the modal/compositional enrichment in the lithosphere for a time interval as long as 50 Ma, i.e. from the Variscan subduction to the Mid-Triassic magmatism, can be matter of debate. In particular, it is complicated by the Permian (~294 to 274 Ma) onset of a large magmatic phase, during which mantle-derived anhydrous basaltic melts with tholeiitic to subduction-related affinity were produced by the SCLM and/or the asthenosphere (Sinigoi et al., 2016; Boscaini et al., 2020). These magmas underplated the thick crustal piles and induced extensive anatexis, leading to the emplacement of mafic/ultramafic to granitic/rhyolitic rocks throughout the Ivrea-Verbano Zone, particularly in Val Sesia (Voshage et al., 1990; Sinigoi et al., 2016; Karakas et al., 2019) and the Athesina Volcanic District (Barth

et al., 1993; Marocchi et al., 2008). Furthermore, the gabbroic bodies of the Finero Mafic Complex record the intrusion of multiple discrete tholeiitic/transitional magmatic batches between Permian and Triassic, suggesting the existence of a multi-stage thermal evolution for the Southern Alps lithosphere (Lu et al., 1997; Zanetti et al., 2013; Langone et al., 2017). In this framework, the timing between the enrichment of Southern Alps SCLM and the Mid-Triassic shoshonitic magmatism can belong to two different scenarios:

a) The existence of a Triassic arc/back-arc system at the NW Paleotethys limb (Zanetti et al., 2013). In this view, the infiltration of slab-derived components into a depleted SCLM would promote the formation of a Finero-like suprasubductive mantle domain during Mid-Triassic, making the shoshonitic magmatism a simple expression of an active subduction-related setting. This model implies that the enriched signature related to the Variscan subduction in the Southern Alps SCLM was exhausted by the voluminous Permian magmatic event (see Storck et al., 2020).

b) The preservation, in the Southern Alps lithospheric mantle, of an enrichment induced by the Variscan subduction (Bonadiman et al., 1994; Zanetti et al., 1999; Lustrino et al., 2019). In this view, the SCLM would have been capable of generating a transitional to alkaline magmatic phase delayed with respect to the metasomatic events. The Sr-Nd isotopes support the plausibility of such a scenario, showing how the hypothetical slab-derived components (i.e. GLOSS/GLOSS-II), the Finero peridotite, the metasomatic amphiboles and the Mid-Triassic magmatic rocks would lie on the same mixing curve (Fig. 7). This hypothesis is also in line with the model of Pilet et al. (2015), according to whom continental rift-related Na- to K-alkaline magmatism could be decoupled from the metasomatic enrichment of the underlying mantle source. Analogous speculations were made by Panter et al. (2018) to model the Cenozoic (48-30 Ma) alkaline magmatism of the West Antartic Rift System by melting of amphibole-rich metasomes generated in the SCLM during the 550-150 Ma Ross subduction. In an analogous way, the shoshonitic magmatism of the Southern Alps would have been generated by a Finero-

like mantle source, and would represent the exhaustion of the Variscan subduction-related signature in the Southern Alps SCLM that predated the Late Triassic-Early Jurassic opening of the Alpine Tethys (Fig. 11).

10. Conclusive remarks

A comprehensive study of the acme of the Middle Triassic shoshonitic magmatism in the Dolomites enabled us to constrain the nature and evolution of the Southern Alps SCLM between the Variscan subduction and the opening of the Alpine Tethys. Insights from major/trace elements and Sr-Nd isotopes were brought together to frame the shoshonitic magmatism into a comprehensive picture at both local and regional geodynamic scale. The main points are summarized here:

- The shoshonitic magmatism in the Southern Alps at 239-237 Ma is mostly represented by a huge effusive phase, during which SiO_2-saturated (SS) to SiO_2-unsaturated (SU) melts partially crystallized and differentiated *en route* to the surface. The *T-P* paths recorded by olivine and clinopyroxene phenocrysts in the least differentiated rocks encompass a considerable interval, spanning from 1200-1210 °C at 830 MPa to 1010-1060 °C at 160-230 MPa (i.e. polybaric crystallization during ascent). At 160-230 MPa, almost isobaric crystallization conditions marked the onset of differentiation in discrete magma batches at shallow crustal levels, the remnants of which are still visible in the Predazzo-Mt. Monzoni plutons (Bonadiman et al., 1994; Casetta et al., 2018a).
- The primary transitional to alkali basaltic SS and SU melts in equilibrium with a fertile SCLM were generated by 5-7% partial melting of a metasomatised amphibole+phlogopite-bearing spinel lherzolite similar to the Finero peridotite. Such a source was probably located at depth of 40-60 km, consistent with theoretical (Selverstone and Sharp, 2011) and experimental data (e.g., Conceição and Green, 2004).

- The metasomatic modification of the Mid-Triassic Southern Alps SCLM by slab-related components (Fig. 7) derived from the Variscan subduction could have been preserved into the Southern Alps SCLM, being able to induce the shoshonitic magmatic phase during Mid-Triassic (Fig. 11).
- The modelled Finero-like mantle sources are capable of retaining up to 600-800 ppm H_2O, resulting in the production of primary transitional to alkali basaltic SS/SU melts with ~1.1 wt% H_2O. The shoshonitic magmatism of the Dolomites could fix at 237-239 Ma the exhaustion of the Variscan subduction-related signature in the Southern Alps SCLM. This event predated the Late Triassic onset of a major rifting phase related to the opening of the Alpine Tethys, the expression of which are recorded in small volume alkaline magmas (e.g., Casetta et al., 2019).

Funding

This work was supported by The University Institute for Higher Studies (IUSS) Mobility Research Programme of the University of Ferrara [grant numbers 570, 571] for Long Period, 2016/2017 to [FC], and the Italian National Research Program [PRIN_2017 Project 20178LPCPW] to [MC].

Acknowledgements

Anne Kelly and Vincent Gallagher are thanked for making the Sr and Nd isotopic analyses at SUERC. Renzo Tamoni (University of Ferrara) is acknowledged for his help during thin section preparation. Authors are grateful to Andrea Marzoli and an anonymous reviewer for their constructive comments, which improved an earlier version of the manuscript. Michael Roden is acknowledged for his careful editorial handling and guidance.

References

Barth, S., Oberli, F., Meier, M., Blattner, P., Bargossi, G.M., Di Battistini, G., 1993. The evolution of a calc-alkaline basic to silicic magma system: Geochemical and Rb-Sr, Sm-Nd, and $^{18}O/^{16}O$ isotopic evidence from the Late Hercynian Atesina-Cima d'Asta volcano-plutonic complex, northern Italy. Geochimica et Cosmochimica Acta 57(17), 4285-4300.

Bernoulli, D., Lemoine, M., 1980. Birth and Early Evolution of the Tethys: the Overall Situation. Mémoires du Bureau de Recherches Géologiques et Minières 115, 168-179.

Bianchini, G., Natali, C., Shibata, T., Yoshikawa, M., 2018. Basic dykes crosscutting the crystalline basement of Valsugana (Italy): new evidence of early Triassic volcanism in the Southern Alps. Tectonics 37(7), 2080-2093.

Bonadiman, C., Coltorti, M., Siena, F., 1994. Petrogenesis and *T*-fO_2 estimates of Mt. Monzoni complex (Central Dolomites, Southern Alps): a Triassic shoshonitic intrusion in a trascurrent geodynamic setting. European Journal of Mineralogy 6, 943-966.

Boscaini, A., Marzoli, A., Davies, J. F., Chiaradia, M., Bertrand, H., Zanetti, A., ..., Jourdan, F., 2020. Permian post-collisional basic magmatism from Corsica to the Southeastern Alps. Lithos, 376, 105733.

Carraro, A., Visonà, D., 2003. Mantle xenoliths in Triassic camptonite dykes of the Predazzo Area (Dolomites, Northern Italy). European Journal of Mineralogy 15(1), 103-115.

Casetta, F., Coltorti, M., Ickert, R.B., Bonadiman, C., Giacomoni, P.P., Ntaflos, T. (2018a). Intrusion of shoshonitic magmas at shallow crustal depth: *T*-*P* path, H_2O estimates, and AFC modeling of the Middle Triassic Predazzo Intrusive Complex (Southern Alps, Italy). Contributions to Mineralogy and Petrology 173(7), 57.

Casetta, F., Coltorti, M., Marrocchino, E., 2018b. Petrological evolution of the Middle Triassic Predazzo Intrusive Complex, Italian Alps. International Geology Review 60(8), 977-997.

Casetta, F., Ickert, R.B., Mark, D.F., Bonadiman, C., Giacomoni, P.P., Ntaflos, T., Coltorti, M., 2019. The alkaline lamprophyres of the Dolomitic Area (Southern Alps, Italy): markers of

775 the Late Triassic change from orogenic-like to anorogenic magmatism. Journal of Petrology
776 60(6), 1263-1298.
777 Casetta, F., Giacomoni, P.P., Ferlito, C., Bonadiman, C., Coltorti, M., 2020. The evolution of
778 the mantle source beneath Mt. Etna (Sicily, Italy): from the 600 ka tholeiites to the recent
779 trachybasaltic magmas. International Geology Review 62(3), 338-359.
780 Coltorti, M., Siena, F., 1984. Mantle tectonite and fractionate peridotite at Finero (Italian
781 Western Alps). Neues Jahrbuch fur Mineralogie-Abhandlungen 149(3), 225-244.
782 Conceição, R.V., Green, D.H., 2004. Derivation of potassic (shoshonitic) magmas by
783 decompression melting of phlogopite+ pargasite lherzolite. Lithos 72(3-4), 209-229.
784 Condamine, P., Médard, E., 2014. Experimental melting of phlogopite-bearing mantle at 1 GPa:
785 Implications for potassic magmatism. Earth and Planetary Science Letters 397, 80-92.
786 Conticelli, S., Guarnieri, L., Farinelli, A., Mattei, M., Avanzinelli, R., Bianchini, G., ...,
787 Venturelli, G., 2009. Trace elements and Sr–Nd–Pb isotopes of K-rich, shoshonitic, and
788 calc-alkaline magmatism of the Western Mediterranean Region: genesis of ultrapotassic to
789 calc-alkaline magmatic associations in a post-collisional geodynamic setting. Lithos 107(1-
790 2), 68-92.
791 De Min, A., Velicogna, M., Ziberna, L., Chiaradia, M., Alberti, A., Marzoli, A., 2020. Triassic
792 magmatism in the European Southern Alps as an early phase of Pangea break-up. Geological
793 Magazine, 1-23.
794 Doglioni, C., 2007. Tectonics of the Dolomites. Bulletin für angewandte Geologie 12(2), 11-
795 15.
796 Falloon, T.J., Green, D.H., 1988. Anhydrous partial melting of peridotite from 8 to 35 kb and
797 the petrogenesis of MORB. Journal of Petrology 1, 379-414.
798 Faure, G., 1986. Principles of isotope geology. John Wiley and Sons, Inc., New York, NY.
799 Gaetani, G.A., Grove, T.L., 1998. The influence of water on melting of mantle peridotite.
800 Contributions to Mineralogy and Petrology 131(4), 323-346.

Giacomoni, P.P., Bonadiman, C., Casetta, F., Faccini, B., Ferlito, C., Ottolini, L., Zanetti, A., Coltorti, M., 2020. Long-term storage of subduction-related volatiles in Northern Victoria Land lithospheric mantle: insight from olivine-hosted melt inclusions from McMurdo basic lavas (Antarctica). Lithos 105826.

Giovanardi, T., Zanetti, A., Dallai, L., Morishita, T., Hémond, C., Mazzucchelli, M., 2020. Evidence of subduction-related components in sapphirine-bearing gabbroic dykes (Finero phlogopite-peridotite): Insights into the source of the Triassic-Jurassic magmatism at the Europe-Africa boundary. Lithos 356, 105366.

Hao, Y.T., Bonadiman, C., Coltorti, M., Xia, Q.K., 2019. Fragments of asthenosphere incorporated in the lithospheric mantle underneath the Subei Basin, eastern China; constraints from geothermobarometric results and water contents of peridotite xenoliths in Cenozoic basalts. Journal of Asian Earth Science 1, 100006.

Hartmann, G., Wedepohl, K.H., 1993. The composition of peridotite tectonites from the Ivrea Complex, northern Italy: residues from melt extraction. Geochimica et Cosmochimica Acta 57(8), 1761-1782.

Ickert, R.B., 2013. Algorithms for estimating uncertainties in initial radiogenic isotope ratios and model ages. Chemical Geology 340, 131-138.

Ionov, D.A., Bigot, F., Braga, R., 2017. The provenance of the lithospheric mantle in continental collision zones: petrology and geochemistry of peridotites in the Ulten-Nonsberg Zone (Eastern Alps). Journal of Petrology 58(7), 1451-1472.

Karakas, O., Wotzlaw, J.F., Guillong, M., Ulmer, P., Brack, P., Economos, R., ..., Bachmann, O., 2019. The pace of crustal-scale magma accretion and differentiation beneath silicic caldera volcanoes. Geology 47(8), 719-723.

Kessel, R., Schmidt, M.W., Ulmer, P., Pettke, T., 2005. Trace element signature of subduction-zone fluids, melts and supercritical liquids at 120-180 km depth. Nature 437(7059), 724-727.

827 Kress, V.C., Carmichael, I.S., 1991. The compressibility of silicate liquids containing Fe_2O_3
828 and the effect of composition, temperature, oxygen fugacity and pressure on their redox
829 states. Contributions to Mineralogy and Petrology 108(1-2), 82-92.
830 Kroner, U., Romer, R.L., 2014. Anatomy of a diffuse cryptic suture zone: an example from the
831 Bohemian Massif, European Variscides: comment. Geology 42(7), e340-e340.
832 Langone, A., José, A.P.N., Ji, W.Q., Zanetti, A., Mazzucchelli, M., Tiepolo, M., ..., Bonazzi,
833 M., 2017. Ductile-brittle deformation effects on crystal-chemistry and U-Pb ages of
834 magmatic and metasomatic zircons from a dyke of the Finero Mafic Complex (Ivrea–
835 Verbano Zone, Italian Alps). Lithos 284, 493-511.
836 Lanzafame, G., Casetta, F., Giacomoni, P.P., Donato, S., Mancini, L., Coltorti, M., ..., Ferlito,
837 C., 2020. The Skaros effusive sequence at Santorini (Greece): Petrological and geochemical
838 constraints on an interplinian cycle. Lithos 362-363, 105504.
839 Le Maitre, R.W., Bateman, P., Dudek, A., Keller, J., Lameyre, L., Sabine, P. A., ..., Zanettin,
840 B., 1989. A classification of igneous rocks and glossary of terms: recommendations of the
841 IUGS Commission on the Systematics of Igneous Rocks. Cambridge University Press, pp.
842 254.
843 Liu, X. I., O'Neill, H.S.C., Berry, A.J., 2006. The effects of small amounts of H_2O, CO_2 and
844 Na_2O on the partial melting of spinel lherzolite in the system CaO-MgO-Al_2O_3-
845 SiO_2±H_2O±CO_2±Na_2O at 1.1 GPa. Journal of Petrology 47(2), 409-434.
846 Lu, M., Hofmann, A.W., Mazzucchelli, M., Rivalenti, G., 1997. The mafic-ultramafic complex
847 near Finero (Ivrea-Verbano Zone), I. Chemistry of MORB-like magmas. Chemical Geology
848 140(3-4), 207-222.
849 Lugmair, G. W., Marti, K., 1978. Lunar initial $^{143}Nd/^{144}Nd$: differential evolution of Lunar crust
850 and mantle. Earth and Planetary Science Letters 39, 349-357.

Lustrino, M., Abbas, H., Agostini, S., Caggiati, M., Carminati, E., Gianolla, P., 2019. Origin of Triassic magmatism of the Southern Alps (Italy): Constraints from geochemistry and Sr-Nd-Pb isotopic ratios. Gondwana Research 75, 218-238.

Malitch, K.N., Belousova, E.A., Griffin, W.L., Badanina, I.Y., Knauf, V.V., O'Reilly, S.Y., Pearson, N.J., 2017. Laurite and zircon from the Finero chromitites (Italy): New insights into evolution of the subcontinental mantle. Ore Geology Reviews 90, 210-225.

Mandler, B.E., Grove, T.L., 2016. Controls on the stability and composition of amphibole in the Earth's mantle. Contributions to Mineralogy and Petrology 171(8-9), 68.

Marocchi, M., Morelli, C., Mair, V., Klötzli, U., Bargossi, G.M., 2008. Evolution of large silicic magma systems: new U-Pb zircon data on the NW Permian Athesian Volcanic Group (Southern Alps, Italy). The Journal of Geology 116(5), 480-498.

Mazzucchelli, M., Zanetti, A., Rivalenti, G., Vannucci, R., Correia, C.T., Tassinari, C.C.G., 2010. Age and geochemistry of mantle peridotites and diorite dykes from the Baldissero body: Insights into the Paleozoic-Mesozoic evolution of the Southern Alps. Lithos 119(3-4), 485-500.

McDonough, W.S., 1990. Constraints on the composition of the continental lithospheric mantle. Earth and Planetary Science Letters 101(1), 1-18.

Melchiorre, M., Faccini, B., Grégoire, M., Benoit, M., Casetta, F., Coltorti, M., 2020. Melting and metasomatism/refertilisation processes in the Patagonian sub-continental lithospheric mantle: A review. Lithos 354, 105324.

Morimoto, N., 1988. Nomenclature of pyroxenes. Mineralogy and Petrology 39(1), 55-76.

Morishita, T., Hattori, K.H., Terada, K., Matsumoto, T., Yamamoto, K., Takebe, M., ..., Arai, S., 2008. Geochemistry of apatite-rich layers in the Finero phlogopite–peridotite massif (Italian Western Alps) and ion microprobe dating of apatite. Chemical Geology 251(1-4), 99-111.

876 Mukasa, S.B., Shervais, J.W., 1999. Growth of subcontinental lithosphere: evidence from
877 repeated dike injections in the Balmuccia lherzolite massif, Italian Alps. Lithos, 48(1-4),
878 287-316.
879 Panter, K.S., Castillo, P., Krans, S., Deering, C., McIntosh, W., Valley, J.W., ..., Blusztajn, J.,
880 2018. Melt origin across a rifted continental margin: a case for subduction-related
881 metasomatic agents in the lithospheric source of alkaline basalt, NW Ross Sea, Antarctica.
882 Journal of Petrology 59(3), 517-558.
883 Peccerillo, A., Frezzotti, M.L., 2015. Magmatism, mantle evolution and geodynamics at the
884 converging plate margins of Italy. Journal of the Geological Society 172(4), 407-427.
885 Peccerillo, A., Taylor, S.R., 1975. Geochemistry of Upper Cretaceous volcanic rocks from the
886 Pontic chain, northern Turkey. Bulletin volcanologique 39(4), 557.
887 Perinelli, C., Mollo, S., Gaeta, M., De Cristofaro, S.P., Palladino, D.M., Armienti, P., ...,
888 Putirka, K.D., 2016. An improved clinopyroxene-based hygrometer for Etnean magmas and
889 implications for eruption triggering mechanisms. American Mineralogist 101(12), 2774-
890 2777.
891 Pilet, S., 2015. Generation of low-silica alkaline lavas: Petrological constraints, models, and
892 thermal implications. The interdisciplinary Earth: A volume in Honor of Don L. Anderson:
893 Geological Society of America Special Papers 514, 281-304.
894 Plank, T., 2014. The chemical composition of subducting sediments. Elsevier.
895 Pouchou, J.L., Pichoir, F., 1991. Quantitative analysis of homogeneous or stratified
896 microvolumes applying the model “PAP”, in: Electron probe quantitation. Springer US, pp.
897 31-75.
898 Putirka, K.D., Johnson, M., Kinzler, R., Longhi, J., Walker, D., 1996. Thermobarometry of
899 mafic igneous rocks based on clinopyroxene-liquid equilibria, 0-30 kbar. Contributions to
900 Mineralogy and Petrology 123(1), 92-108.

Putirka, K.D., Mikaelian, H., Ryerson, F., Shaw, H., 2003. New clinopyroxene-liquid thermobarometers for mafic, evolved, and volatile-bearing lava compositions, with applications to lavas from Tibet and the Snake River Plain, Idaho. American Mineralogist 88(10), 1542-1554.

Putirka, K.D., 2008. Thermometers and barometers for volcanic systems. Reviews in Mineralogy and Geochemistry 69(1), 61-120.

Roeder, P.L., Emslie, R., 1970. Olivine-liquid equilibrium. Contributions to Mineralogy and Petrology 29(4), 275-289.

Rotenberg, E., Davis, D.W., Amelin, Y., Ghosh, S., Bergquist, B.A., 2012. Determination of the decay-constant of ^{87}Rb by laboratory accumulation of ^{87}Sr. Geochimica et Cosmochimica Acta 85, 41-57.

Saccani, E., 2015. A new method of discriminating different types of post-Archean ophiolitic basalts and their tectonic significance using Th-Nb and Ce-Dy-Yb systematics. Geoscience Frontiers 6(4), 481-501.

Schmid, S.M., Fügenschuh, B., Kounov, A., Maţenco, L., Nievergelt, P., Oberhänsli, R., ..., Ustaszewski, K., 2020. Tectonic units of the Alpine collision zone between Eastern Alps and western Turkey. Gondwana Research 78, 308-374.

Selverstone, J., Sharp, Z.D., 2011. Chlorine isotope evidence for multicomponent mantle metasomatism in the Ivrea Zone. Earth and Planetary Science Letters 310(3-4), 429-440.

Shaw, D.M., 1979. Trace element melting models. Physics and Chemistry of the Earth 11, 577-586.

Sinigoi, S., Quick, J.E., Demarchi, G., Klötzli, U.S., 2016. Production of hybrid granitic magma at the advancing front of basaltic underplating: Inferences from the Sesia Magmatic System (south-western Alps, Italy). Lithos 252, 109-122.

Sloman, L.E., 1989. Triassic shoshonites from the dolomites, northern Italy: Alkaline arc rocks in a strike-slip setting. Journal of Geophysical Research: Solid Earth 94(B4), 4655-4666.

927 Smith, E.I., Sanchez, A., Walker, J.D., Wang, K., 1999. Geochemistry of mafic magmas in the
928 Hurricane Volcanic field, Utah: implications for small-and large-scale chemical variability
929 of the lithospheric mantle. The Journal of Geology 107(4), 433-448.
930 Stahle, V., Frenzel, G., Hess, J.C., Saupé, F., Schmidt, S.T., Schneider, W., 2001. Permian
931 metabasalt and Triassic alkaline dykes in the northern Ivrea zone: clues to the post-Variscan
932 geodynamic evolution of the Southern Alps. Schweizerische Mineralogische und
933 Petrographische Mitteilungen 81(1), 1-21.
934 Stampfli, G.M., Hochard, C., Vérard, C., Wilhem, C., 2013. The formation of Pangea.
935 Tectonophysics 593, 1-19.
936 Storck, J.C., Wotzlaw, J.F., Karakas, Ö., Brack, P., Gerdes, A., Ulmer, P., 2020. Hafnium
937 isotopic record of mantle-crust interaction in an evolving continental magmatic system.
938 Earth and Planetary Science Letters 535, 116100.
939 Sun, S., McDonough, W.F., 1989. Chemical and isotopic systematics of oceanic basalts:
940 implication for mantle and processes, in: Saunders, A.D., Norry, M.J. (Eds.), Magmatism in
941 the Ocean Basins. Geological Society of London, Special Publications 42, 313-345.
942 Tiepolo, M., Bottazzi, P., Palenzona, M., Vannucci, R., 2003. A laser probe coupled with ICP-
943 double-focusing sector-field mass spectrometer for in situ analysis of geological samples
944 and U-Pb dating of zircon. The Canadian Mineralogist 41(2), 259-272.
945 Tommasi, A., Langone, A., Padrón-Navarta, J.A., Zanetti, A., Vauchez, A., 2017. Hydrous
946 melts weaken the mantle, crystallization of pargasite and phlogopite does not: Insights from
947 a petrostructural study of the Finero peridotites, Southern Alps. Earth and Planetary Science
948 Letters 477, 59-72.
949 Traill, R.J., Lachance, G.R., 1966. A practical solution to the matrix problem in X-ray analysis.
950 II. Application to a multicomponent alloy system. Canadian Spectroscopy 11(3), 63-71.

951 Tumiati, S., Thöni, M., Nimis, P., Martin, S., Mair, V., 2003. Mantle-crust interactions during
952 Variscan subduction in the Eastern Alps (Nonsberg–Ulten zone): geochronology and new
953 petrological constraints. Earth and Planetary Science Letters 210(3-4), 509-526.
954 Voshage, H., Hunziker, J.C., Hofmann, A.W., Zingg, A., 1987. A Nd and Sr isotopic study of
955 the Ivrea zone, Southern Alps, N-Italy. Contributions to Mineralogy and Petrology 97, 31-
956 42.
957 Voshage, H., Hofmann, A.W., Mazzucchelli, M., Rivalenti, G., Sinigoi, S., Raczek, I.,
958 Demarchi, G., 1990. Isotopic evidence from the Ivrea Zone for a hybrid lower crust formed
959 by magmatic underplating. Nature 347(6295), 731-736.
960 Wood, D.A., 1980. The application of a Th-Hf-Ta diagram to problems of tectonomagmatic
961 classification and to establishing the nature of crustal contamination of basaltic lavas of the
962 British Tertiary Volcanic Province. Earth and Planetary Science Letters 50(1), 11-30.
963 Workman, R.K., Hart, S.R., 2005. Major and trace element composition of the depleted MORB
964 mantle (DMM). Earth and Planetary Science Letters 231(1), 53-72.
965 Wotzlaw, J.F., Brack, P., Storck, J.C., 2018. High-resolution stratigraphy and zircon U–Pb
966 geochronology of the Middle Triassic Buchenstein Formation (Dolomites, northern Italy):
967 precession-forcing of hemipelagic carbonate sedimentation and calibration of the Anisian-
968 Ladinian boundary interval. Journal of the Geological Society 175(1), 71-85.
969 Zanetti, A., Mazzucchelli, M., Rivalenti, G., Vannucci, R., 1999. The Finero phlogopite-
970 peridotite massif: an example of subduction-related metasomatism. Contributions to
971 Mineralogy and Petrology 134(2-3), 107-122.
972 Zanetti, A., Mazzucchelli, M., Sinigoi, S., Giovanardi, T., Peressini, G., Fanning, M., 2013.
973 SHRIMP U–Pb Zircon Triassic intrusion age of the Finero mafic complex (Ivrea–Verbano
974 zone, Western Alps) and its geodynamic implications. Journal of Petrology 54(11), 2235-
975 2265.

976 Zanetti, A., Giovanardi, T., Langone, A., Tiepolo, M., Wu, F.Y., Dallai, L., Mazzucchelli, M.,
977 2016. Origin and age of zircon-bearing chromitite layers from the Finero phlogopite
978 peridotite (Ivrea-Verbano Zone, Western Alps) and geodynamic consequences. Lithos 262,
979 58-74.
980 Zheng, Y.F., 2019. Subduction zone geochemistry. Geoscience Frontiers 10(4), 1223-1254.
981 Zindler, A., Hart, S.R., 1986. Chemical geodynamics. Annual Review of Earth and Planetary
982 Sciences 14, 493-571.
983

984 **Figure captions**

985 **Fig. 1. (colour online)**

986 (a) Map of the tectonic units of the eastern portion of the Alps (modified from Schmid et al.,
987 2020). LO: Ligurian Ophiolites; AM: deformed Adriatic margin; AD: Adriatic Microplate; SA:
988 Southern Alps; DI: Dinarides; SM: Southern margin of Meliata; HB: Eoalpine High-Pressure
989 Belt; TW: Tauern tectonic Window; EW: Engadine tectonic Window; OTW: Ossola-Tessin
990 tectonic Window; EA: Eastern Austroalpine; H: Helvetic domain; M: Molasse foredeep. The
991 Mid-Triassic magmatic occurrences in the Southern Alps domain are evidenced in black. (b)
992 Basaltic trachyandesitic dyke intruded in the volcanic sequences. (c) Ultramafic xenoliths
993 embedded in a trachybasaltic dyke. (d) Simplified geological map of the volcano-plutonic
994 sequences and dyke swarm cropping out near Predazzo (modified from Casetta et al., 2018a).
995 SS = Shoshonitic Silica Saturated; SU = Shoshonitic Silica Undersaturated; GU = Granitic Unit.
996 Stars indicate dykes where ultramafic xenoliths were found.
997

998 **Fig. 2. (colour online)**

999 Photomicrographs of representative thin sections of the studied lavas, dykes and ultramafic
1000 cumulates. (a) Triple junctions between clinopyroxene grains in a clinopyroxenitic xenolith. (b)
1001 Contact between a clinopyroxenitic xenoliths and the host SU trachybasaltic dyke. (c) Highly

porphyritic SS trachybasaltic dyke. (d, e) Clinopyroxene, olivine and plagioclase phenocrysts in a SU trachybasaltic dyke; (f) Highly porphyritic SS trachybasaltic lava. Cpx: clinopyroxene; Plg: plagioclase; Sp: spinel. (a), (b), (d) and (e) are in transmitted cross-polarized light; (c) and (f) are in transmitted plane-polarized light. Scale bar is 1 mm.

Fig. 3. (colour online)

(a) TiO_2 (wt%) vs. Mg# and (b) Wollastonite (Wo)-Enstatite (En)-Ferrosilite (Fs) (Morimoto, 1988) diagrams for clinopyroxene in lavas, dykes and clinopyroxenites. (c, d) Chondrite-normalized (Sun and McDonough, 1989) incompatible element and REE patterns of clinopyroxene in clinopyroxenites. The composition of clinopyroxene near the contact with the host SU dyke is also discriminated. The major and incompatible element distribution of clinopyroxene phenocrysts in the Late Triassic lamprophyric dykes from the same area (Casetta et al., 2019) is also reported for comparison.

Fig. 4. (colour online)

Major and trace element compositions of SS lavas and SS/SU dykes. (a) Total Alkali vs. Silica (TAS) (Le Maitre et al., 2002), (b) K_2O (wt%) vs. SiO_2 (wt%) (Peccerillo and Taylor, 1975), (c) CaO/Al_2O_3 vs. SiO_2 (wt%), and (d) Ni (ppm) vs. MgO (wt%) diagrams. The composition of the SS, SU and GU bodies of the Predazzo Intrusive Complex (PIC) and of the Late Triassic lamprophyric dykes from the same area (Casetta et al., 2018a; 2018b; 2019) are also reported for comparison. Asterisks indicate the composition of the primary SS transitional basalt and SU alkali basalt resulted from the backward fractionation models (see text).

Fig. 5. (colour online)

(a, b) Primitive Mantle- (PM) and Chondrite-normalized (Sun and McDonough, 1989) incompatible element and REE diagrams showing the composition of the SS lavas, SS/SU

dykes and clinopyroxenites. (c, d) Primitive Mantle- (PM) and Chondrite-normalized incompatible element and REE patterns of the primary SS transitional basalt and SU alkali basalt resulted from the backward fractionation models. The patterns of the Late Triassic lamprophyres from the same area (Casetta et al., 2019) are also reported for comparison in (c) and (d).

Fig. 6. (colour online)

Trace element discrimination diagrams for the studied SS lavas and SS/SU dykes in comparison with the Late Triassic lamprophyres from the same area (Casetta et al., 2019). (a) Th_N vs. Nb_N (Saccani, 2015), (b) Nb/La vs. La/Yb diagrams (Smith et al., 1999) and (c) Th-Hf-Ta ternary diagram (Wood, 1980).

Fig. 7. (colour online)

$^{87}Sr/^{86}Sr$ vs. $^{143}Nd/^{144}Nd$ diagram for the studied SS lavas and SS/SU dykes (corrected to 238 Ma) compared to the Permian Campore dyke (280 Ma; Sinigoi et al., 2016), Ulten peridotite (330 Ma; Tumiati et al., 2003), Finero phlogopite peridotite (FPP, 300 Ma; Voshage et al., 1987), metasomatic amphiboles in the FPP (300 Ma; Giovanardi et al., 2020, and references therein), and the Southern Alps basement (gneisses, paragneisses, stronalites, 300-330 Ma; Voshage et al., 1990; Tumiati et al., 2003; Sinigoi et al., 2016). Fields indicate the composition of Balmuccia-Baldissero peridotites (Voshage et al., 1987; Mukasa and Shervais, 1999), Southern Alps Mid-Triassic magmatic rocks (Lustrino et al., 2019) and the Predazzo Intrusive Complex (PIC) SS/SU rocks (Casetta et al., 2018a). DMM = depleted MORB mantle (Workman and Hart, 2005; corrected to 238 Ma); EM I = enriched mantle (Zindler and Hart, 1986); GLOSS and GLOSS-II = average global subducting sediments (Plank, 2014); Average crust = average composition of the Southern Alps Permo-Triassic crust (Voshage et al., 1990; Tumiati et al., 2003; Sinigoi et al., 2016). Curves represent the mixing trends between DMM

and GLOSS, GLOSS-II and the Permo-Triassic average crust. Numbers indicate the mixing percentages.

Fig. 8. (colour online)

Chondrite-normalized (Sun and McDonough, 1989) incompatible element patterns of the inferred Mid-Triassic mantle sources that generated SS/SU magmas. SS- and SU-like sources are constituted by 96% DMM + 4% GLOSS-II and 98% DMM + 2% GLOSS components, respectively. Whole-rock patterns of FPP (Giovanardi et al., 2020), Ulten peridotites (Ionov et al., 2017), DMM (Workman and Hart, 2005), PM (Sun and McDonough, 1989) and Etna-like enriched mantle (EM; Casetta et al., 2020) are also reported.

Fig. 9. (colour online)

Chondrite-normalized (Sun and McDonough, 1989) incompatible element diagrams showing the composition of the modelled (a) SS and (b) SU mantle sources and primary melts. In each panel, the composition of the mantle source obtained by mass balance calculations and that resulted from the mixing models are indicated. The composition of the primary (a) SS transitional basalt and (b) SU alkali basalt and of the melt generated at 7% and 5% partial melting from the corresponding sources are also indicated.

Fig. 10. (colour online)

(a) $^{Cpx\text{-}melt}Kd_{Fe\text{-}Mg}$ vs. Mg# diagram for clinopyroxene crystals in equilibrium (or brought to the equilibrium) with the SS and SU melts. The equilibrium range indicated by the black lines ($^{Cpx\text{-}melt}Kd_{Fe\text{-}Mg}$ = 0.24-0.30) is from Putirka et al. (2003). (b) Chondrite-normalized (Sun and McDonough, 1989) incompatible element pattern of the hypothetical melt in equilibrium with clinopyroxene grains in clinopyroxenite (see Supplementary Material for the partition coefficients) compared to that of the natural SS trachybasaltic dyke. (c) Temperature (*T*, °C)

1080 vs. pressure (*P*, MPa) diagram showing the clinopyroxene crystallization conditions in the
1081 SS/SU magmas, and the corresponding melt H_2O content of the melts. The maximum *T-P*
1082 crystallization interval of the Late Triassic lamprophyres (Casetta et al., 2019; De Min et al.,
1083 2020) is also reported in (c).
1084
1085 **Fig. 11. (colour online)**
1086 Evolutionary sketch of the Southern Alps SCLM between Carboniferous and Late Triassic,
1087 adapted from Pilet (2015) and Panter et al. (2018). (a) Carboniferous (>320 Ma) subduction of
1088 the Paleotethys beneath the Adria plate resulting in the slab-derived metasomatism of the
1089 Southern Alps SCLM (Stampfli et al., 2013). (b) Permian extensional stage activated by
1090 brittle/ductile intra-lithospheric shear zones inducing thinning, partial melting of the SCLM.
1091 This resulted in the production of tholeiitic to calc-alkaline magmas which intruded the Lower
1092 Crust, and induced the hybrid anatectic to mafic-derived acidic magmatism throughout the
1093 Ivrea-Verbano Zone and the Athesina Volcanic District. (c) Middle Triassic prolounged
1094 extensional phase inducing the exhaustion of the slab-derived enrichment retained in the
1095 SCLM, and resulting in the production of calc-alkaline to shoshonitic magmatism. (d) Late
1096 Triassic production of alkaline magmas throughout the Southern Alps caused by the rift-related
1097 asthenospheric upwelling predating the opening of the Alpine Tethys.

Figure 1

Click here to access/download;Figure;Fig. 1.tif

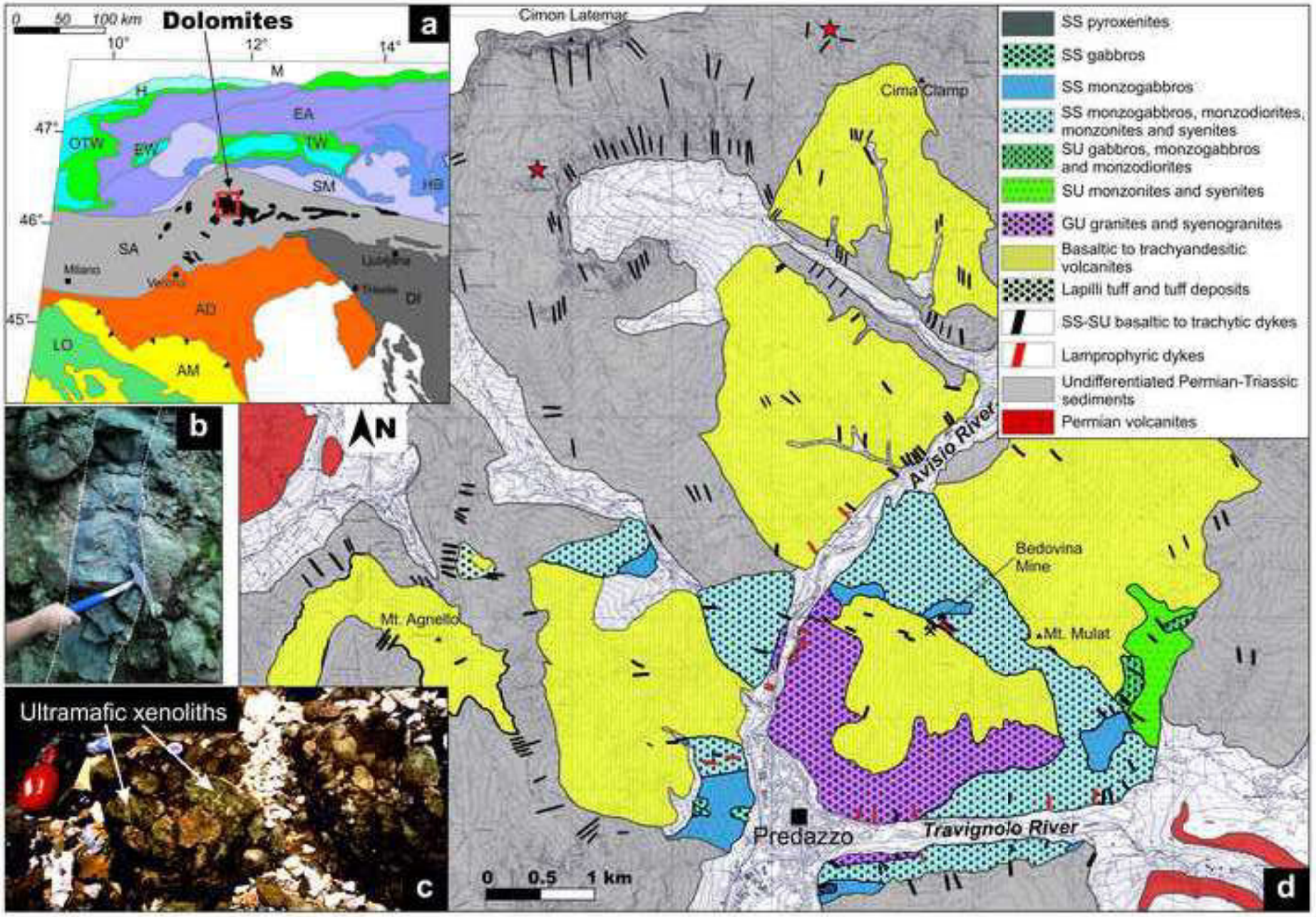

Figure 2

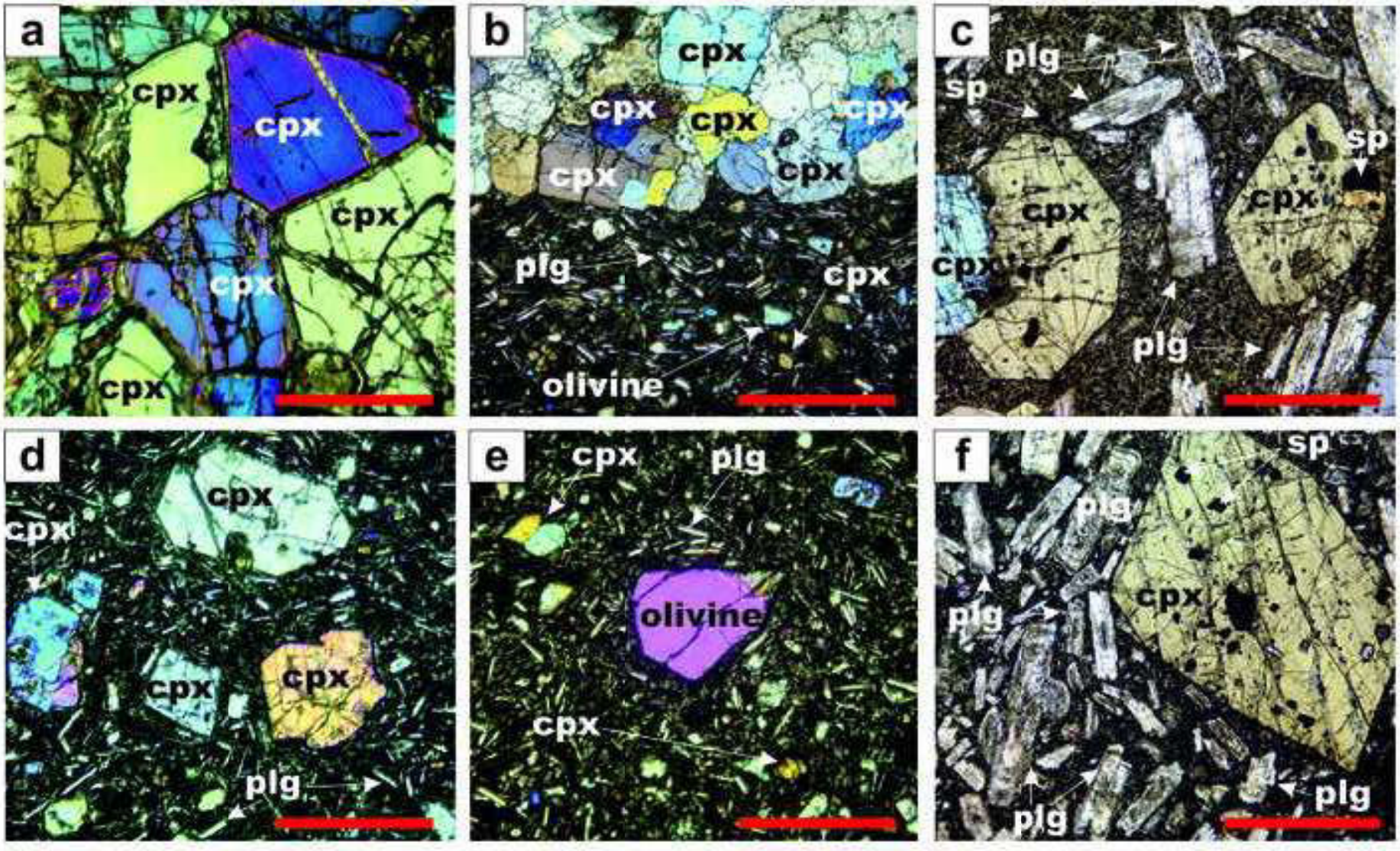

Figure 3

Click here to access/download;Figure;Fig. 3.tif

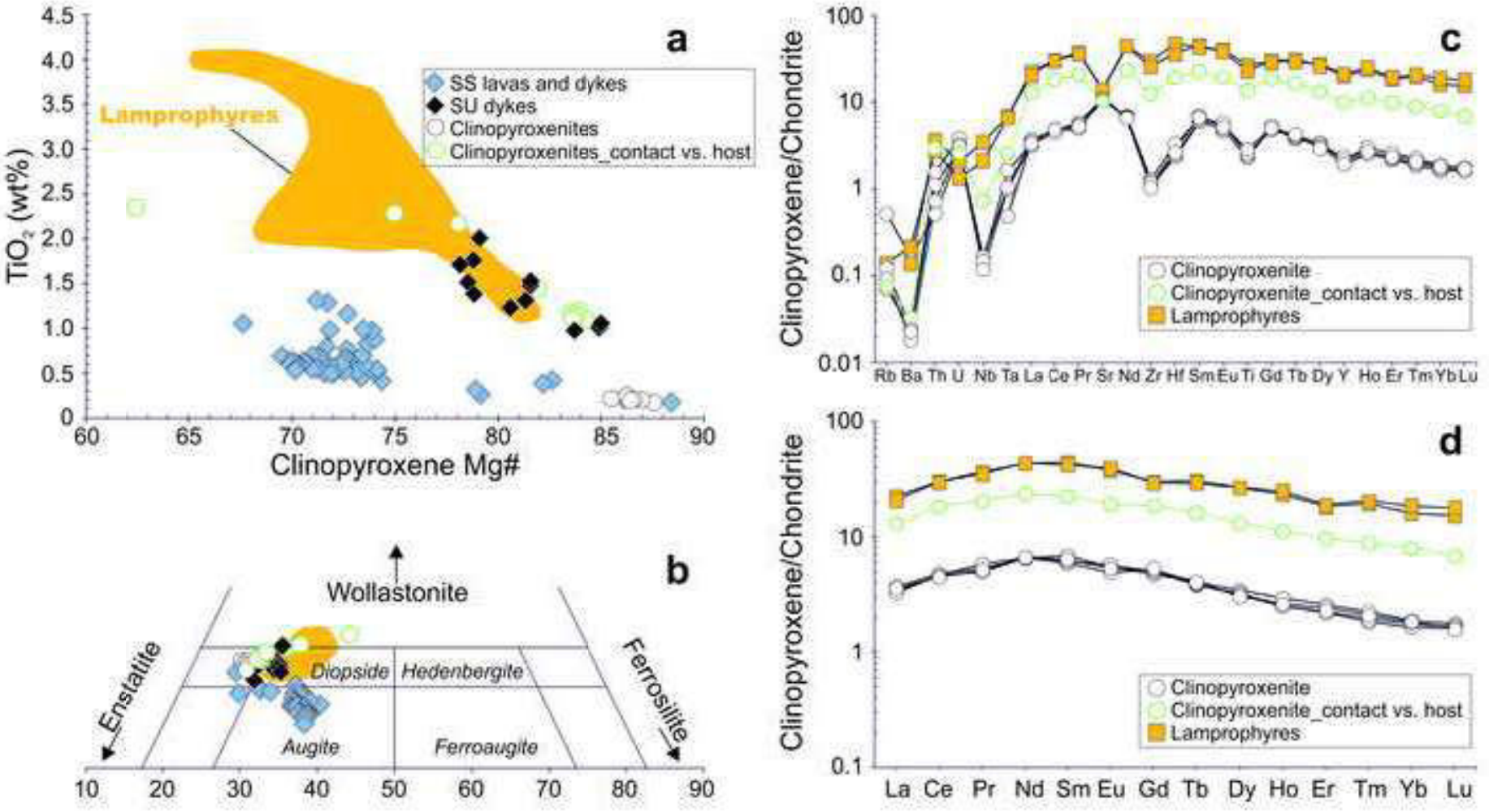

Figure 4

Click here to access/download;Figure;Fig. 4.tif

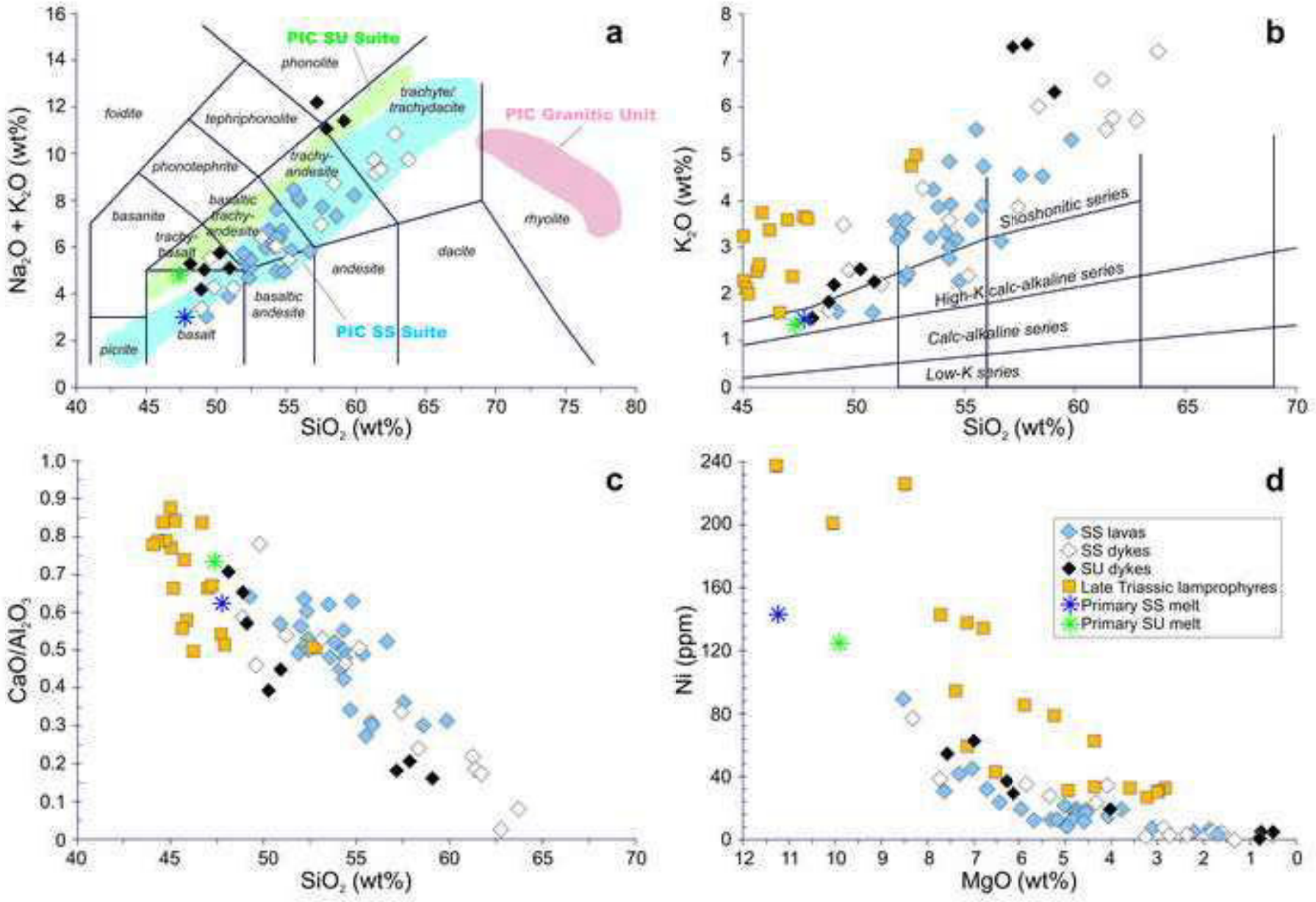

Figure 5

Click here to access/download;Figure;Fig. 5.tif

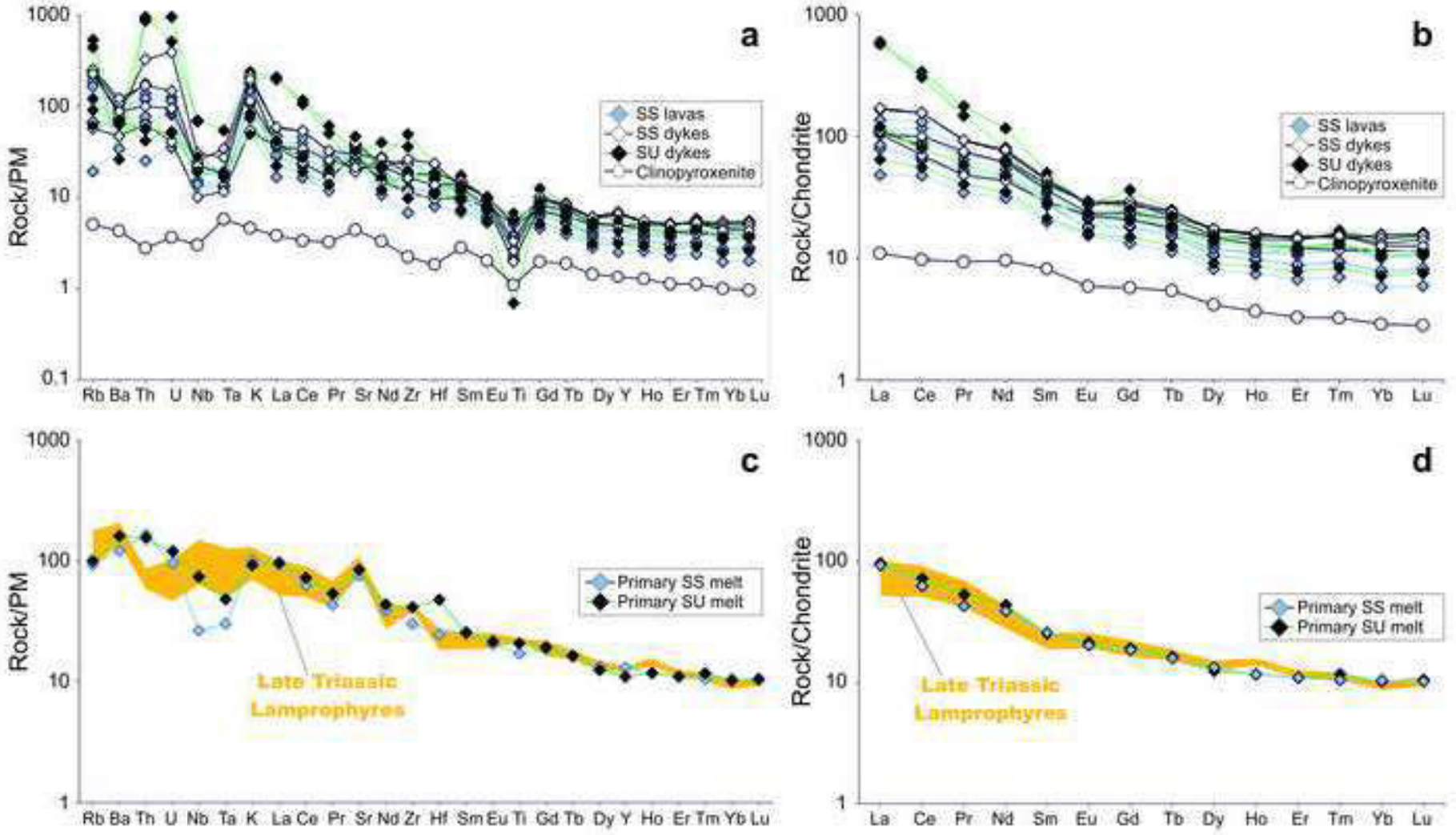

Figure 6

Click here to access/download;Figure;Fig. 6.tif

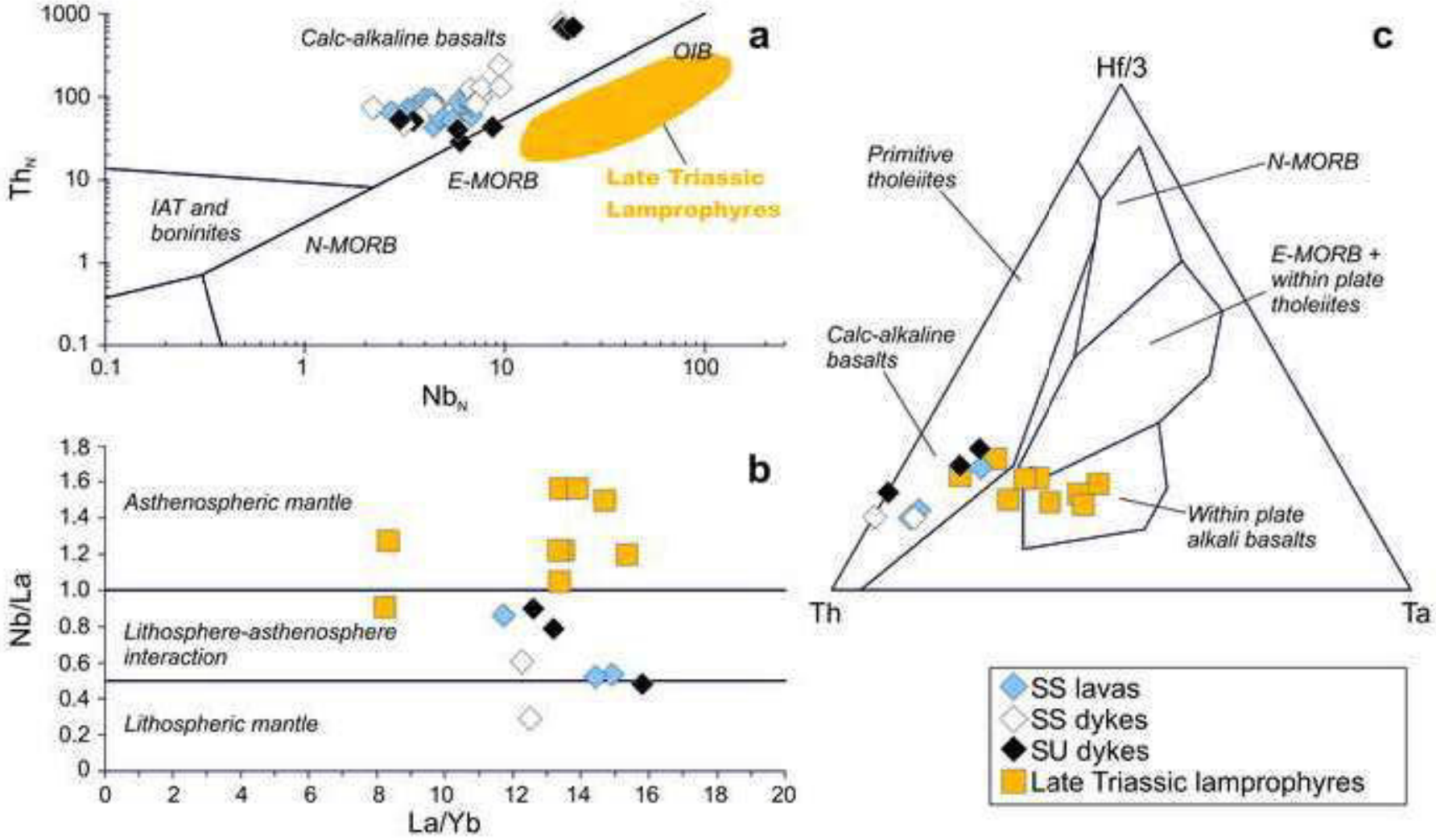

Figure 7

Click here to access/download;Figure;Fig. 7.tif

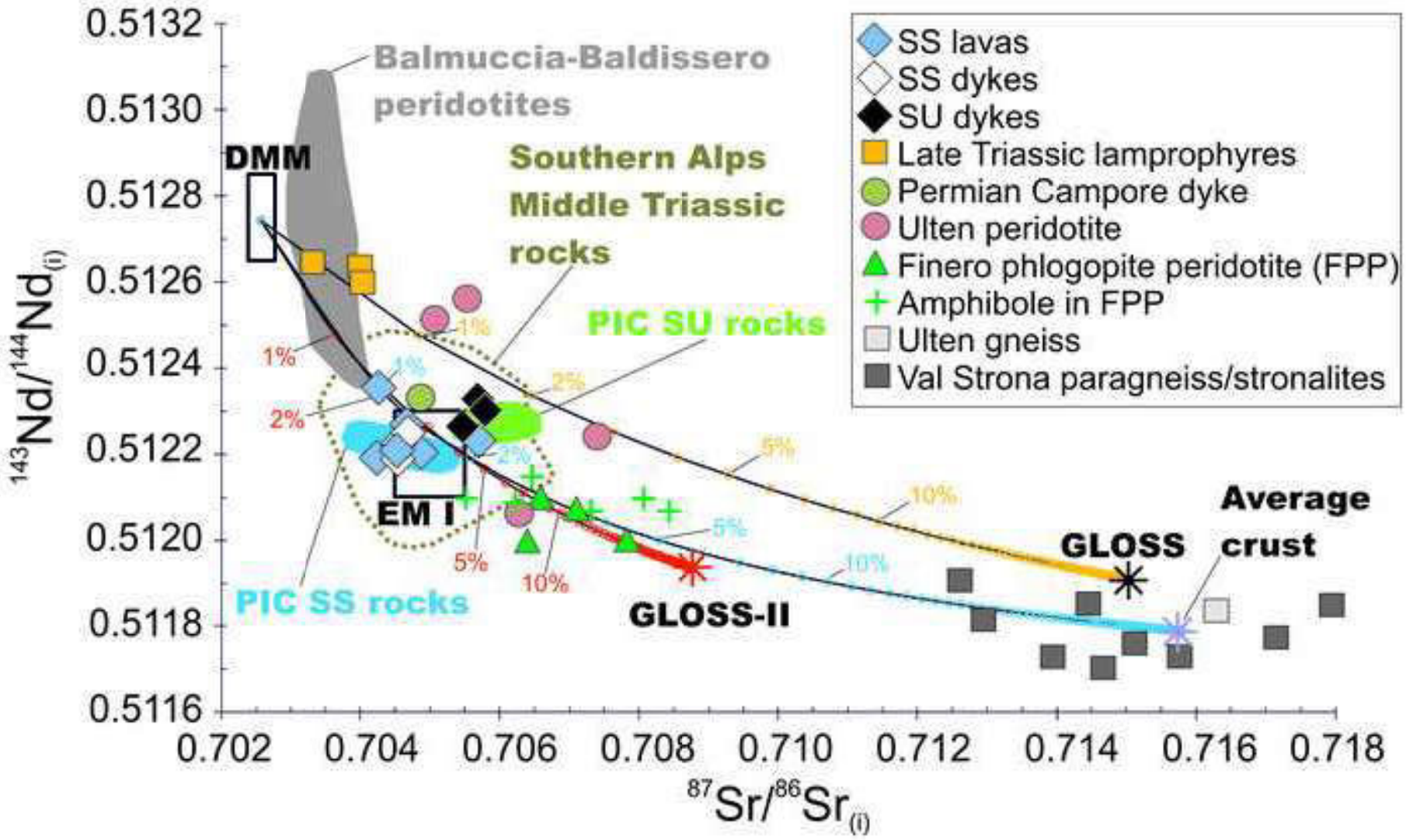

Figure 8

Click here to access/download;Figure;Fig. 8.tif

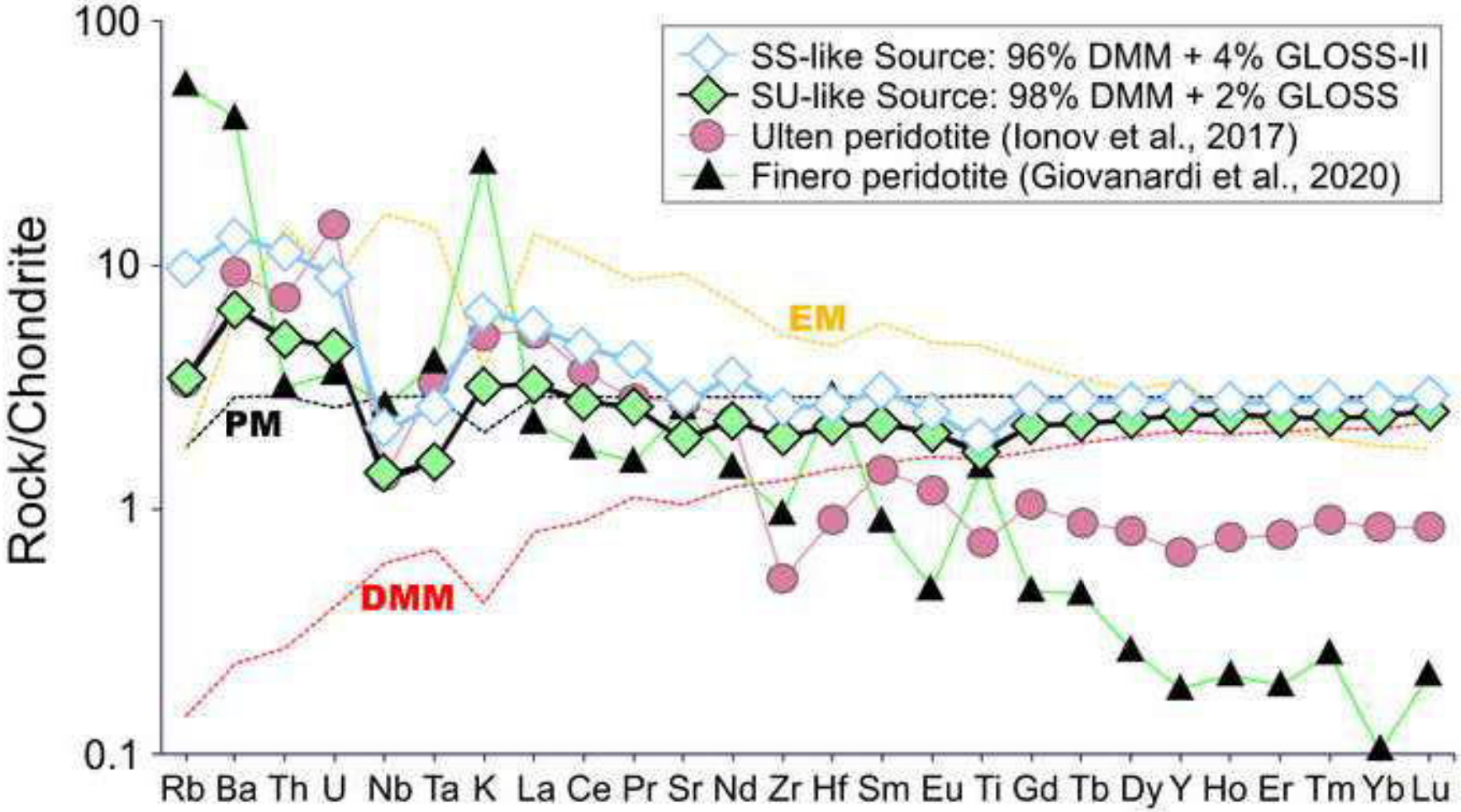

Figure 9

Click here to access/download;Figure;Fig. 9.tif

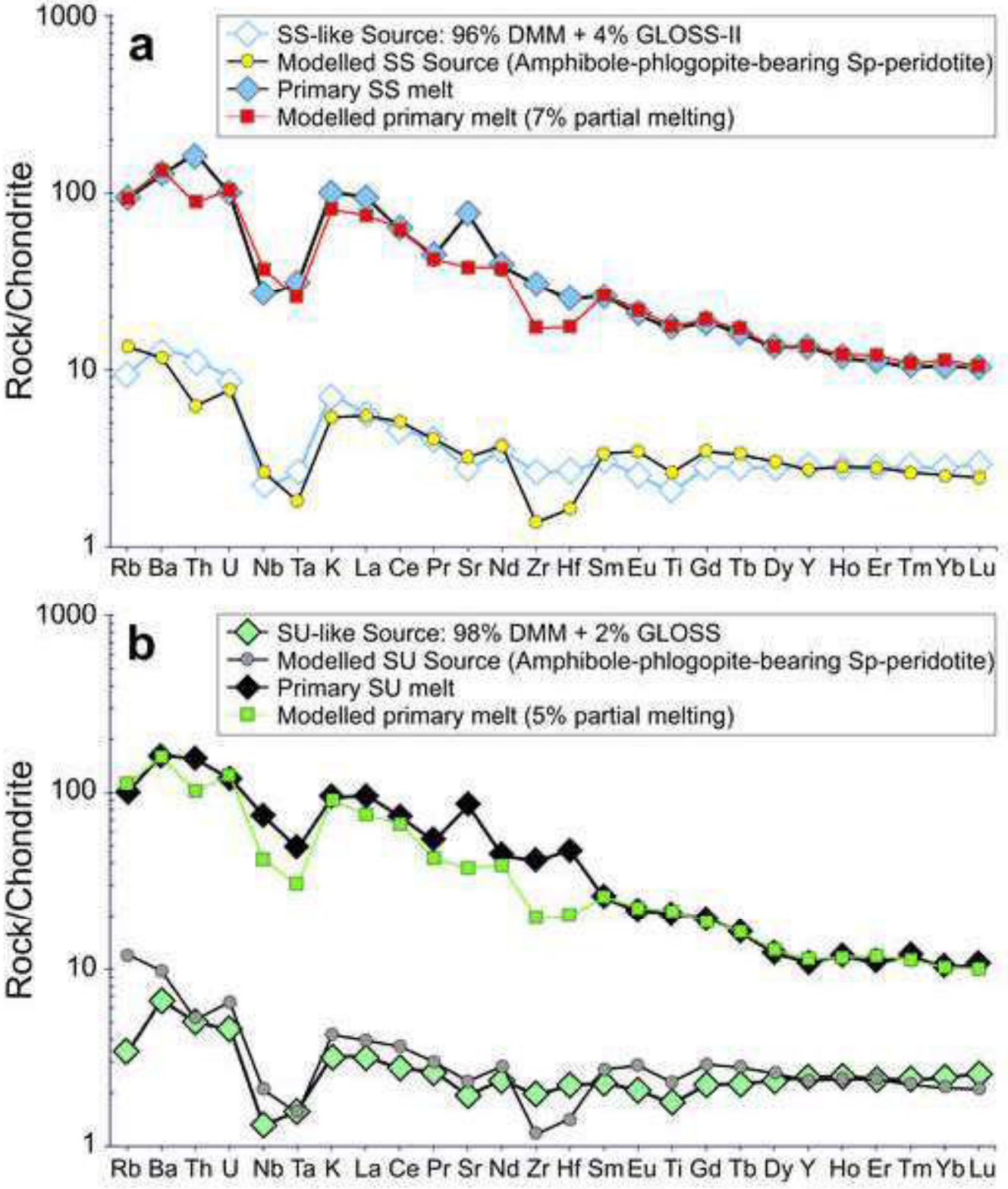

Figure 10

Click here to access/download;Figure;Fig. 10.tif

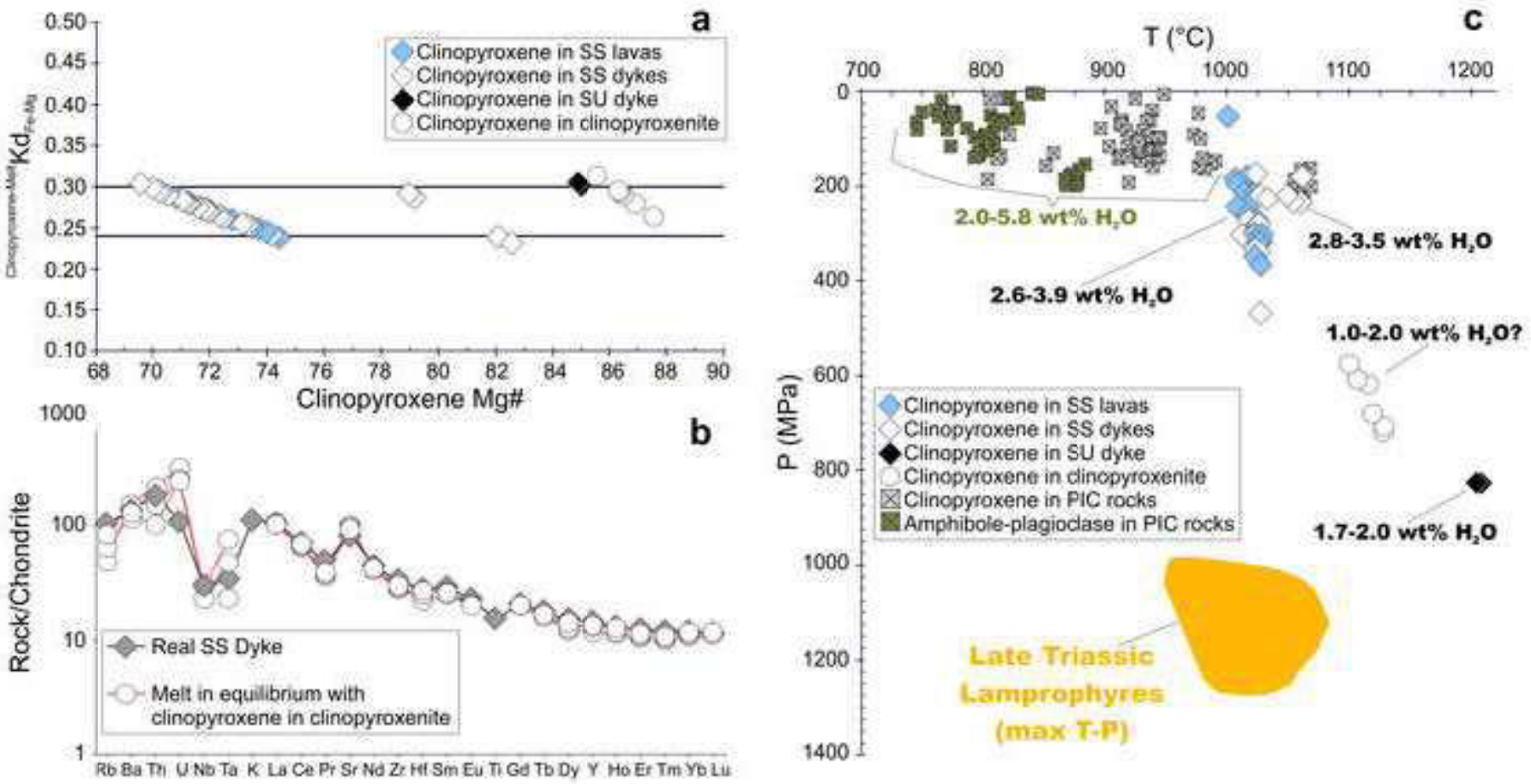

Figure 11

Click here to access/download;Figure;Fig. 11.tif

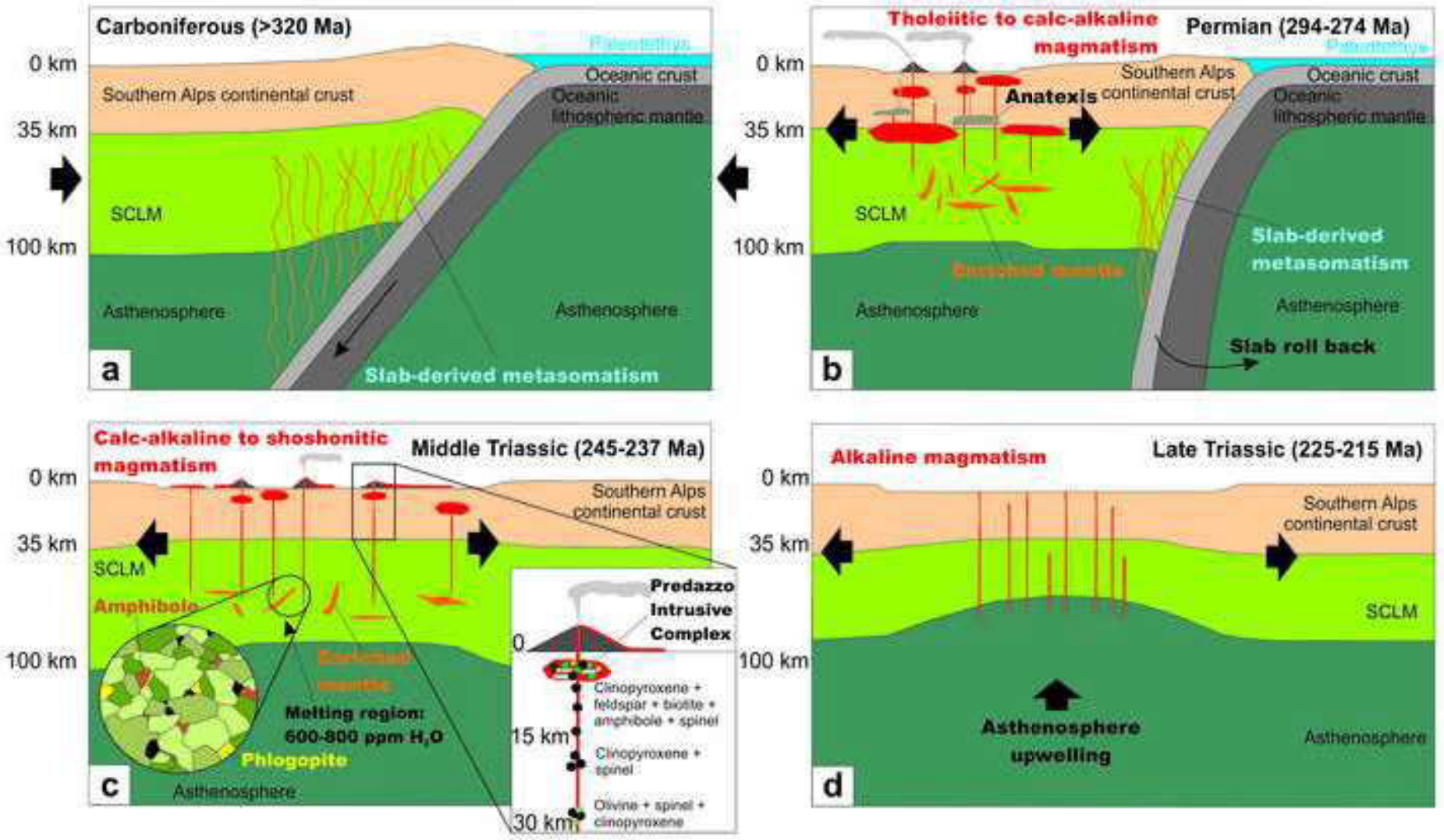

Table 1 Whole rock major, trace element composition and $^{87}Sr/^{86}Sr$ and $^{143}Nd/^{144}Nd$ isotopes of representative lavas, dykes and ultramafic cumulates from the Predazzo area (Dolomites, Southern Alps). Fe_2O_3 and FeO were calculated by considering a Fe_2O_3/ FeO ratio of 0.15, in agreement with a fO_2 around FMQ buffer (Kress and Carmichael, 1991). Mg# = Mg/[Mg+Fe^{2+}] mol%; n.d. = not detected; LOI = Loss On Ignition. All trace element (ppm) were analysed by ICP-MS except Pb, Zn, Ni, Co, Cr, V and Ba (XRF). The trace element composition of samples labelled with (*) was entirely determined by XRF. Sr-Nd isotopic ratios were corrected for 238 Ma of radiogenic ingrowth using the trace element abundances determined by ICP-MS, the decay rates of Rotenberg et al. (2012) and Lugmair and Marti (1978). Initial ratios (i) and uncertainties (2σ) were propagated according to Ickert (2013). P.I. = Porphyricity Index; SS = Silica-saturated; SU = Silica-undersaturated; Tr-bas = Trachybasalt; Bas tr-and = Basaltic trachyandesite; Tr-and = Trachyandesite; Tra = Trachyte; Cpxite = Clinopyroxenite.

Lithology	**Tr-bas**	**Tr-bas**	**Tr-bas**	**Bas tr-and**	**Bas tr-and**	**Bas tr-and**	**Bas tr-and**	**Bas tr-and**	**Bas tr-and**	**Tr-and**	**Tr-and**	**Tr-and**	**Tr-bas**	**Tr-bas**	**Tr-bas**
Type	**Lava**	**Lava**	**Lava**	**Lava**	**Lava**	**Lava**	**Lava**	**Lava**	**Lava**	**Lava**	**Lava**	**Lava**	**Dyke**	**Dyke**	**Dyke**
Suite	SS	SS	SS	SS	SS	SS	SS	SS	SS	SS	SS	SS	SS	SS	SS
P.I. (%)	45-50	25-30	40-45	5-10	55-60	30-35	30-35	35-40	35-40	25-30	20-25	20-25	25-30	40-45	25-30
Sample	**FC39**	**A43 (*)**	**A54 (*)**	**A11 (*)**	**FC7**	**A12**	**FC9**	**FC10 (*)**	**FC43 (*)**	**FC14**	**FC44**	**A22 (*)**	**A46**	**A75 (*)**	**EM93**
SiO_2 (wt%)	50.25	51.42	48.56	54.12	51.41	53.07	53.06	52.69	52.97	59.30	57.15	57.28	48.13	48.98	47.33
TiO_2	1.27	0.86	1.17	0.86	0.85	0.79	0.79	1.18	0.82	0.49	0.57	0.51	1.11	0.83	1.08
Al_2O_3	16.59	16.36	16.55	16.53	15.15	17.19	14.40	16.50	15.60	18.36	18.23	19.35	17.75	14.38	18.57
Fe_2O_3	1.22	1.26	1.24	1.23	1.15	1.12	1.19	1.12	1.09	0.62	0.83	0.69	1.16	1.36	1.10
FeO	8.10	8.39	8.33	8.24	7.68	7.48	7.94	7.49	7.29	4.14	5.51	4.58	7.71	9.08	7.36
MnO	0.15	0.22	0.17	0.18	0.17	0.21	0.17	0.17	0.23	0.11	0.09	0.19	0.14	0.19	0.12
MgO	7.53	5.87	8.40	5.11	6.62	3.99	6.38	7.06	5.22	1.70	2.19	1.82	8.18	7.60	5.58
CaO	9.45	8.30	10.63	5.65	9.63	7.75	8.94	8.75	8.13	5.75	6.61	5.85	10.41	11.22	8.58
Na_2O	2.26	2.12	1.41	3.53	2.22	2.68	2.76	2.73	2.82	2.90	3.18	2.76	1.72	1.76	1.97
K_2O	1.57	3.26	1.61	3.13	3.23	3.24	3.19	2.45	3.80	5.26	4.52	4.42	1.62	2.45	3.32
P_2O_5	0.32	0.52	0.54	0.40	0.37	0.46	0.33	0.34	0.43	0.43	0.44	0.33	0.51	0.49	0.46
LOI	1.81	1.18	1.67	1.25	0.61	1.26	0.55	0.65	1.53	0.79	0.87	0.79	2.04	0.70	3.82
Total	100.52	99.76	100.28	100.23	99.09	99.24	99.70	101.13	99.93	99.85	100.19	98.57	100.48	99.04	99.29
Mg#	**62.3**	**55.5**	**64.2**	**52.5**	**60.6**	**48.7**	**58.9**	**62.7**	**56.1**	**42.2**	**41.4**	**41.5**	**65.4**	**59.8**	**57.4**
Pb (ppm)	15.8	24.7	6.40	15.5	14.1	36.6	16.80	12.6	14.8	30.0	19.3	31.7	7.40	7.9	5.2
Zn	90.5	132.5	86.7	117	70.1	213	70.5	73.9	99.1	64	52.6	170.3	73.6	96.1	51.2
Ni	31.4	19.7	89.4	12.6	32.5	15.8	23.9	45.3	12.9	3.30	5.30	6.50	77.3	38.5	35.3
Co	31.6	29.7	38.1	35.1	35.0	28.8	31.3	30.6	24.6	33.7	7.8	10.6	30.3	53.5	25.6
Cr	45.8	82.4	201	17.2	101.7	44.5	166	94.8	117	0.80	4.70	8.40	128	238	49.8
V	255	192	262	207	258	202	231	212	193	62	92	82.4	225	292	221
Rb	12.4	115	38.2	121	41.7	106	43.3	70.3	122	136	119	143	36.5	65.2	146
Ba	243	556	395	615	455	518	505	393	556	676	621	679	331	531	620
Sr	541	722	597	608	513	682	550	712	689	793	813	1012	613	611	855
Nb	10.0	7.9	6.4	7.8	10.0	13.6	10.9	12.9	13.9	16.6	15.4	14.4	7.30	5.20	16.0
Zr	76.7	148	158	145	132	139	143	173	150	267	195	206	130	116	184
Hf	2.49				3.54	4.12	3.58			5.83	5.23		2.96		4.26
U	0.75				1.72	2.43	1.80			1.95	2.65		0.87		1.99
Th	2.18	6.70	7.60	8.20	5.70	10.5	6.60	6.00	10.30	10.20	11.90	9.70	5.40	8.60	8.53
Y	11.4	26.8	24.5	24.0	14.7	23.2	16.1	27.4	31.7	19.7	22.8	26.7	23.0	23.7	30.7
Ta	0.48				0.54	0.75	0.57			0.80	0.76		0.48		n.d.
La	11.6	27.9	26.5	18.2	18.9	28.4	20.3	28.7	47.7	27.0	32.7	58.1	24.9	6.00	26.5
Ce	29.6	62.5	51.3	61.2	39.3	55.6	41.3	49.0	71.1	71.4	81.3	70.1	43.2	50.9	51.5
Pr	3.31				4.83	6.89	5.15			6.18	7.11		4.59		n.d.
Nd	14.63				20.47	28.28	21.64			24.94	28.39		20.4		30.2
Sm	3.06				4.13	5.49	4.32			4.66	5.23		4.47		6.23
Eu	0.89				1.07	1.26	1.05			1.22	1.25		1.32		1.71
Gd	2.76				3.68	4.86	3.82			4.23	4.74		4.29		5.62
Tb	0.43				0.56	0.75	0.59			0.63	0.70		0.67		0.91
Dy	2.09				2.69	3.58	2.76			3.06	3.32		3.80		4.46
Ho	0.43				0.55	0.73	0.56			0.64	0.69		0.74		0.92
Er	1.11				1.44	1.94	1.48			1.76	1.86		2.03		2.42
Tm	0.18				0.24	0.32	0.24			0.30	0.31		0.30		0.40
Yb	0.98				1.31	1.79	1.36			1.71	1.79		1.99		2.16
Lu	0.15				0.21	0.27	0.21			0.27	0.28		0.29		0.32
$^{87}Sr/^{86}Sr$	0.704490				0.705460	0.707224	0.705615			0.705941	0.705990				0.706349
$^{87}Rb/^{86}Sr$	0.0662				0.2352	0.4502	0.2277			0.4971	0.4246				0.4951
$^{87}Sr/^{86}Sr$(i)	0.704270				0.704677	0.705725	0.704857			0.704286	0.704576				0.704700
2σ	0.000020				0.000017	0.000027	0.000019			0.000020	0.000027				0.000025
$^{143}Nd/^{144}Nd$	0.512548				0.512465	0.512424	0.512392			0.512363	0.512392				0.512447
$^{147}Sm/^{144}Nd$	0.1264				0.1221	0.1173	0.1207			0.1128	0.1114				0.1245
$^{143}Nd/^{144}Nd$(i)	0.512351				0.512275	0.512241	0.512204			0.512187	0.512218				0.512253
2σ	0.000006				0.000051	0.000006	0.000007			0.000019	0.000007				0.000006

Table 1 (continued)

Lithology	**Bas tr-and**	**Bas tr-and**	**Tr-and**	**Tr-and**	**Tra**	**Tra**	**Tra**	**Tr-bas**	**Tr-bas**	**Tr-bas**	**Tr-bas**	**Tra**	**Tra**	**Cpxite**
Type	**Dyke**	**Dyke**	**Dyke**	**Dyke**	**Dyke**	**Dyke**	**Dyke**	**Dyke**	**Dyke**	**Dyke**	**Dyke**	**Dyke**	**Dyke**	**Xenolith**
Suite	SS	SS	SS	SS	SS	SS	SS	SU	SU	SU	SU	SU	SU	SS
P.I. (%)	25-30	5-10	50-55	5-10	10-15	35-40	15-20	5-10	45-50	25-30	45-50	5-10	20-25	-
Sample	**EM80A**	**P96B (*)**	**EM35 (*)**	**FC41A**	**A23 (*)**	**A96**	**FC54**	**CT55**	**EM51 (*)**	**A61**	**A47 (*)**	**EM104**	**EM11**	**CT8**
SiO_2 (wt%)	53.78	51.75	56.61	57.46	62.55	58.82	60.67	46.75	47.76	48.37	49.54	52.84	56.80	51.67
TiO_2	0.88	0.85	1.08	0.71	0.60	0.54	0.43	1.44	1.28	1.16	1.19	0.14	0.44	0.24
Al_2O_3	16.38	16.27	17.81	16.39	16.71	16.64	18.14	16.68	16.52	18.96	20.12	21.54	20.58	2.51
Fe_2O_3	1.29	1.18	0.89	0.97	0.69	0.67	0.50	1.04	1.18	1.07	1.01	0.24	0.43	0.70
FeO	8.58	7.86	5.88	6.50	4.57	4.48	3.35	6.93	7.86	7.14	6.78	1.60	2.84	4.70
MnO	0.18	0.20	0.12	0.16	0.11	0.08	0.24	0.13	0.19	0.15	0.13	0.12	0.13	0.12
MgO	3.96	3.97	2.82	3.19	1.79	1.55	2.70	6.79	7.39	5.90	3.92	0.70	0.50	18.52
CaO	7.59	8.64	6.00	3.93	1.35	3.63	3.36	11.80	10.81	7.49	9.03	3.96	3.35	19.51
Na_2O	2.46	2.08	3.09	2.68	2.54	3.04	3.63	3.72	2.32	3.12	2.79	4.52	4.89	0.20
K_2O	3.54	4.15	3.80	5.92	7.05	6.32	5.45	1.43	1.79	2.42	2.20	6.73	6.08	0.14
P_2O_5	0.39	0.39	0.47	0.51	0.17	0.22	0.28	0.46	0.59	0.40	0.54	0.00	0.07	0.14
LOI	1.73	1.12	1.00	2.38	1.33	3.07	2.59	3.67	1.57	3.78	2.99	7.06	2.98	1.62
Total	100.76	98.46	99.57	100.80	99.46	99.06	101.34	100.84	99.26	99.96	100.24	99.45	99.09	100.07
Mg#	**45.1**	**47.4**	**46.0**	**46.6**	**41.1**	**38.2**	**58.9**	**63.6**	**62.6**	**59.6**	**50.8**	**43.7**	**23.7**	**87.5**
Pb (ppm)	22	17.89	15.80	31.30	19.00	10.90	37.10	5.00	13.70	8.80	10.00	183.00	36.50	6
Zn	130	122	81.2	96.6	77.8	66.5	163	64.0	91.9	130	71.2	551	84.4	25.0
Ni	18.9	34.3	7.60	2.10	4.90	3.80	2.70	62.9	54.7	28.9	19.2	5.00	5.20	104
Co	36.3	33.6	16.50	16.90	6.60	10.3	6.50	36.7	30.7	27.3	21.5	1.00	3.00	41.0
Cr	53.6	59.99	14.00	2.30	4.00	3.00	8.20	266	122	32.0	25.4	2.00	3.50	897
V	205	192	144	97.9	37.3	38.4	39.0	175	274	213	221	12.0	43.8	95.0
Rb	119	116	127	162	196	155	158	39.0	68.6	77.7	58.1	286	344	3.24
Ba	577	678	684	861	849	763	566	434	531	498	473	184	444	30.0
Sr	689	819	685	635	476	404	458	684	631	989	746	421	656	93.78
Nb	10.0	n.d.	17.9	15.9	18.0	18.0	22.0	20.2	7.10	13.7	13.9	49.0	50.6	2.16
Zr	145	169	225	209	278	259	297	177	145	110	218	561	407	24.95
Hf				5.57		n.d.	7.31	5.64		3.37	4.89	7.24	3.67	0.57
U				3.13		n.d.	8.27	1.07		1.07	1.11	20.3	10.8	0.08
Th	9.60	10.2	11.9	14.5	15.0	15.0	28.2	5.02	6.50	4.77	3.59	75.0	81.9	0.24
Y	27.8	25.5	31.2	29.3	33.7	32.1	22.2	19.2	19.1	25.8	14.1	20.0	29.9	6.12
Ta				0.76		1.43	1.13	0.75		n.d.	0.69	n.d.	2.26	0.24
La	41.3	50.4	32.8	40.9	43.2	39.8	24.5	25.6	14.2	28.5	15.4	143	137	2.62
Ce	60.8	75.6	77.3	96.3	103.5	96.0	61.7	49.4	47.2	49.2	34.2	189	209	5.98
Pr				8.96		8.87	7.19	5.64		n.d.	3.88	14.1	17.0	0.90
Nd				36.8		35.1	28.9	22.7		29.6	16.5	38.0	54.8	4.49
Sm				6.84		6.66	5.67	4.33		5.88	3.29	4.43	7.79	1.26
Eu				1.67		1.60	1.37	1.38		1.71	0.94	1.03	1.59	0.34
Gd				6.14		5.97	4.91	4.41		5.23	3.09	5.49	7.50	1.19
Tb				0.91		0.83	0.79	0.68		0.83	0.48	0.58	0.94	0.20
Dy				4.34		4.50	3.94	3.52		3.97	2.33	3.05	4.21	1.07
Ho				0.89		0.87	0.83	0.74		0.81	0.49	0.62	0.88	0.21
Er				2.42		2.53	2.34	2.02		2.09	1.30	1.94	2.50	0.54
Tm				0.40		0.38	0.41	0.33		0.33	0.22	0.35	0.43	0.08
Yb				2.29		2.65	2.47	1.94		1.80	1.22	2.69	2.54	0.49
Lu				0.36		0.40	0.39	0.30		0.27	0.19	0.41	0.37	0.07
$^{87}Sr/^{86}Sr$				0.707044		0.708271	0.708238			0.706576	0.706242	0.712254		0.704715
$^{87}Rb/^{86}Sr$				0.7396		1.1118	0.9970			0.2272	0.2252	1.9677		0.0999
$^{87}Sr/^{86}Sr(i)$				0.704581		0.704568	0.704918			0.705820	0.705492	0.705702		0.704382
2σ				0.000033		0.000053	0.000036			0.000016	0.000022	0.000067		0.000020
$^{143}Nd/^{144}Nd$				0.512405		0.512373	-			0.512484	0.512445	0.512430		-
$^{147}Sm/^{144}Nd$				0.1124		0.1147	-			0.1200	0.1207	0.0705		-
$^{143}Nd/^{144}Nd(i)$				0.512230		0.512194	-			0.512297	0.512257	0.512320		-
2σ				0.000006		0.000008	-			0.000007	0.000006	0.000006		-

Table 2 Major and trace element composition of the calculated SS and SU melts in equilibrium with a fertile mantle assemblage. For each magmatic suite, the starting sample, the amount of backward fractionation (F%) required to reach the primitive composition, the percentage of each fractionated mineral phase and its compositional interval are also indicated. Fo = forsterite; Mg# = Mg/[Mg+Fe^{2+}] mol%; Cr# = Cr/[Cr+Al] mol%.

Calculated primitive melts

Suite	**SS**	**SU**
Composition	**Transitional basalt**	**Alkali basalt**
SiO_2 (wt%)	47.71	47.25
TiO_2	1.26	1.53
Al_2O_3	16.14	15.64
Fe_2O_3	1.28	1.12
FeO	8.56	7.46
MnO	0.16	0.15
MgO	11.23	9.89
CaO	10.07	11.50
Na_2O	1.55	3.45
K_2O	1.46	1.33
P_2O_5	0.46	0.43
Cr_2O_3	0.09	0.23
NiO	0.02	0.02
Total	100.00	100.00
Mg#	**70.0**	**70.3**
Rb (ppm)	32.4	34.9
Ba	293.6	388
Th	4.8	4.49
U	0.8	0.96
Nb	6.5	18.1
Ta	0.4	0.67
La	22.1	22.9
Ce	38.4	44.3
Pr	4.1	5.06
Sr	545.2	614
Nd	18.2	20.4
Zr	115.9	159
Hf	2.6	5.07
Sm	4.0	3.88
Eu	1.2	1.24
Gd	3.8	3.97
Tb	0.6	0.61
Dy	3.4	3.17
Y	20.5	17.2
Ho	0.7	0.67
Er	1.8	1.82
Tm	0.3	0.30
Yb	1.8	1.74
Lu	0.3	0.27

Suite	**SS**	**SU**
Starting sample	**A46**	**CT55**
Backward F%	**11.4**	**10.5**
Olivine	6.9	6.6
Clinopyroxene	3.0	2.4
Spinel	1.5	1.5

Mineral phase compositional interval	
Olivine	Fo = 85-92
Clinopyroxene	Mg# = 86-89
Spinel	Mg# = 7; Cr# = 49

Table 3 Major/trace element and modal composition of the mantle sources modelled by using real mineral phases from the Finero and Baldissero peridotites compared to those of the ideal sources inferred from the Sr-Nd isotopes mixing models (DMM + GLOSS/GLOSS-II; Workman and Hart, 2005; Plank, 2014). The major/trace element composition of the fertile mineral phases from Finero (olivine, orthopyroxene, spinel, amphibole and phlogopite) and Baldissero (clinopyroxene) peridotites used to reconstruct the composition of the SS/SU sources are also reported. The H_2O concentration in the modelled sources, obtained by weighting the H_2O amounts in each mineral phase (according to the estimates made on the Finero peridotite by Tommasi et al., 2017) are also indicated. Olivine, orthopyroxene, spinel and phlogopite compositions are from Giovanardi et al. (2020); clinopyroxene composition is from Mazzucchelli et al. (2010); amphibole composition is from Morishita et al. (2008). * = concentration of trace elements speculated from adjacent elements; ** = U-Th concentrations speculated by considering the maximum amounts reported for clinopyroxene from the Southern Alps orogenic massifs (i.e. Ulten peridotite; Ionov et al., 2017).

	Mantle sources				Mineral phase major/trace element compositions and modal amounts					
	Modelled using real mineral phases		Resulted from mixing models based on Sr-Nd isotopes							
	SS source	SU source	SS source (0.96 DMM + 0.04 GLOSS-II)	SU source (0.98 DMM + 0.02 GLOSS)		Olivine	Orthopyroxene	Clinopyroxene	Spinel	Amphibole	Phlogopite
					Modal amount (SS source)	55.40	23.01	17.71	1.14	1.98	0.76
					Modal amount (SU source)	57.51	24.27	15.1	1.14	1.36	0.62
SiO_2 (wt%)	46.05	45.94	-	-	**SiO_2 (wt%)**	40.80	56.78	51.34	0.00	45.28	39.41
TiO_2	0.20	0.17	-	-	**TiO_2**	0.00	0.12	0.82	0.15	0.42	1.74
Al_2O_3	2.25	1.99	-	-	**Al_2O_3**	0.00	1.49	6.81	30.14	11.06	15.86
FeO_{TOT}	7.53	7.72	-	-	**FeO_{TOT}**	9.27	6.67	2.66	25.06	3.60	2.98
MnO	0.14	0.14	-	-	**MnO**	0.16	0.15	0.09	0.19	0.00	0.00
MgO	38.35	39.30	-	-	**MgO**	49.20	34.05	14.11	11.30	19.00	23.52
CaO	4.23	3.58	-	-	**CaO**	0.01	0.35	21.98	0.00	12.31	0.00
Na_2O	0.30	0.25	-	-	**Na_2O**	0.00	0.00	1.39	0.00	2.36	1.28
K_2O	0.08	0.07	-	-	**K_2O**	0.00	0.00	0.00	0.00	0.74	8.29
Cr_2O_3	0.64	0.61	-	-	**Cr_2O_3**	0.01	0.29	0.82	33.41	1.93	0.57
NiO	0.24	0.23	-	-	**NiO**	0.38	0.07	0.05	0.00	0.00	0.00
Total	100	100	-	-	**Total**	99.83	99.97	100.05	100.25	96.70	93.65
Rb (ppm)	4.66	4.19	3.40	1.19	**Rb (ppm)**	-	7.46	0.04*	-	6.20	370
Ba	28.04	23.80	31.98	16.07	**Ba**	-	29.7	0.05	-	276	2071
Th	0.18	0.15	0.33	0.15	**Th**	-	0.09	0.59**	-	2.90	0.00
U	0.06	0.05	0.07	0.04	**U**	-	0.01	0.29**	-	0.42	0.00
Nb	0.65	0.52	0.52	0.32	**Nb**	-	0.13	2.02	-	11.0	5.46
Ta	0.03	0.02	0.04	0.02	**Ta**	-	0.00	0.10*	-	0.18	0.48
La	1.31	0.93	1.35	0.76	**La**	-	0.03	1.00	-	57.0	0.03
Ce	3.11	2.24	2.83	1.69	**Ce**	-	0.07	3.41	-	126	0.05
Pr	0.38	0.28	0.39	0.25	**Pr**	-	0.01	0.70*	-	13.0	0.01
Sr	23.53	16.89	19.44	14.05	**Sr**	-	1.39	17.04	-	977	112
Nd	1.72	1.31	1.66	1.11	**Nd**	-	0.05	4.37	-	47.0	0.00
Zr	5.34	4.50	10.04	7.58	**Zr**	-	1.05	25.22	-	32.0	0.33
Hf	0.18	0.15	0.29	0.24	**Hf**	-	0.12	0.75*	-	0.85	0.05
Sm	0.51	0.42	0.47	0.35	**Sm**	-	0.04	2.04	-	7.20	0.00
Eu	0.20	0.17	0.15	0.12	**Eu**	-	0.01	0.91	-	1.90	0.04
Gd	0.72	0.60	0.58	0.46	**Gd**	-	0.02	3.41	-	5.50	0.03
Tb	0.13	0.10	0.10	0.08	**Tb**	-	0.01	0.60*	-	0.92	0.00
Dy	0.77	0.65	0.70	0.59	**Dy**	-	0.09	3.77	-	4.30	0.02
Y	4.34	3.64	4.53	3.86	**Y**	-	0.31	21.34	-	25.0	0.01
Ho	0.16	0.13	0.15	0.14	**Ho**	-	0.01	0.80*	-	0.80	0.00
Er	0.46	0.39	0.46	0.40	**Er**	-	0.07	2.27	-	2.30	0.00
Tm	0.07	0.06	0.07	0.06	**Tm**	-	0.02	0.32*	-	0.35	0.00
Yb	0.43	0.36	0.47	0.41	**Yb**	-	0.06	2.12	-	2.20	0.03
Lu	0.06	0.05	0.07	0.07	**Lu**	-	0.01	0.31*	-	0.32	0.00
H_2O (ppm)	784	598	-	-	**H_2O (ppm)**	3.00	111	267.00	-	19300	43000

Table 4 Major, trace element composition and H_2O amount of the SS/SU magmas obtained from partial melting models and mineral phases eutectic melting proprtions. The minimization of the sum of squared residuals between the predicted values for each oxide and the values calculated from the melting models is expressed by the parameter S. Partial melting degrees are expressed as F (%).

	Melting models results	
Suite	**SS**	**SU**
Composition	**Transitional basalt**	**Alkali basalt**
SiO_2 (wt%)	47.98	47.48
TiO_2	1.56	1.60
Al_2O_3	16.58	16.05
FeO_{TOT}	9.06	8.41
MnO	0.04	0.08
MgO	11.50	10.24
CaO	10.01	11.64
Na_2O	1.66	3.00
K_2O	1.17	1.31
Cr_2O_3	0.39	0.16
NiO	0.05	0.03
Total	100.00	100.00
S (should be <1)	**0.98**	**0.44**
Rb (ppm)	33.0	38.9
Ba	329.3	382.8
Th	2.56	2.96
U	0.85	1.00
Nb	9.13	10.32
Ta	0.36	0.42
La	17.8	17.7
Ce	38.8	40.9
Pr	4.03	4.04
Sr	278.4	272.7
Nd	17.8	18.3
Zr	66.2	76.0
Hf	1.86	2.13
Sm	4.03	3.91
Eu	1.27	1.28
Gd	3.93	3.84
Tb	0.63	0.61
Dy	3.42	3.26
Y	21.4	17.9
Ho	0.69	0.66
Er	2.00	1.96
Tm	0.28	0.29
Yb	1.92	1.74
Lu	0.27	0.25
H_2O (wt%)	1.06	1.12

	SS	SU
F (%)	7	5
Eutectic melting proportions		
Olivine	-0.26	-0.11
Orthopyroxene	0.54	0.22
Clinopyroxene	0.32	0.52
Spinel	0.01	-0.02
Amphibole	0.28	0.27
Phlogopite	0.11	0.12
	1.00	1.00

Table 5 *P, T* and H_2O conditions of crystallization of SS and SU magmas recorded by mineral-melt thermobarometric/hygrometric equations. For each adopted method, the chosen equation, corresponding reference and associated error on estimates are reported together with the results interval. The temperature of olivine crystallization was calculated by applying the Putirka et al. (2007) equation. *T* and *P* of clinopyroxene crystallization were obtained by means of the mineral-melt equations of Putirka et al. (2003) and Putirka (2008). The water content of the melt during clinopyroxene crystallization was calculated using the Perinelli et al. (2016) hygrometer. This latter equation was iterated with the Putirka (2008) methods to unveil the T-P-H_2O conditions of crystallization of SS/SU magmas.

Sample	Suite	Method	Phenocryst composition	Reference	T (°C)	Error (°C)	P (MPa)	Error (MPa)	H_2O (wt%)	Error (wt%)
CT55 (trachybasalt)	SU	Olivine-Liq.	Fo 85	Putirka et al. (2007), Eq. 4	1195	±29	-	-	1.5 (input)	-
CT55 (trachybasalt)	SU	Clinopyroxene-Liq.	Mg# 85	Putirka (2008), Eq. 32b/33; Perinelli et al. (2016)	1204-1207	±42	827-829	±260	1.7-2.0	±0.45
CT8 (clinopyroxenite)	SS	Clinopyroxene-Liq.	Mg# 86-88	Putirka et al. (2003); Putirka (2008), Eq. 33	1099-1128	±42	572-714	±170	1.3 (input)	-
A75 (trachybasalt)	SS	Clinopyroxene-Liq.	Mg# 79-83	Putirka (2008), Eq. 32b/33; Perinelli et al. (2016)	1051-1061	±42	181-235	±260	2.8-3.5	±0.45
A75 (trachybasalt)	SS	Clinopyroxene-Liq.	Mg# 70-74	Putirka (2008), Eq. 32b/33; Perinelli et al. (2016)	1012-1035	±42	169-467	±260	2.9-3.8	±0.45
FC39 (trachybasalt)	SS	Clinopyroxene-Liq.	Mg# 71-74	Putirka (2008), Eq. 32b/33; Perinelli et al. (2016)	1016-1028	±42	181-325	±260	2.6-3.2	±0.45
FC7 (basaltic trachyandesite)	SS	Clinopyroxene-Liq.	Mg# 72-74	Putirka (2008), Eq. 32b/33; Perinelli et al. (2016)	1009-1025	±42	246-330	±260	3.4-3.8	±0.45
FC9 (basaltic trachyandesite)	SS	Clinopyroxene-Liq.	Mg# 70-74	Putirka (2008), Eq. 32b/33; Perinelli et al. (2016)	1010-1028	±42	200-368	±260	3.2-3.7	±0.45
FC41 (trachyandesite)	SS	Clinopyroxene-Liq.	Mg# 74	Putirka (2008), Eq. 32b/33; Perinelli et al. (2016)	1001-1008	±42	49-184	±260	3.2-3.8	±0.45

Supplementary material/Appendix (Files for online publication only)

Declaration of Interest Statement

Declaration of interests

☒ The authors declare that they have no known competing financial interests or personal relationships that could have appeared to influence the work reported in this paper.

☐The authors declare the following financial interests/personal relationships which may be considered as potential competing interests:
